

Analytic 3D vector non-uniform Fourier crystal optics in arbitrary $\bar{\bar{\epsilon}}$ dielectric

Chenzhu Xie^{1,2,3} and Yong Zhang^{1,2,3*}

¹*National Laboratory of Solid State Microstructures, Nanjing University, No.15 JinYin Street, Nanjing, 210093, Jiangsu, China.

²*College of Engineering and Applied Sciences, Nanjing University, No.163 Xianlin Avenue, Nanjing, 210046, Jiangsu, China.

³Collaborative Innovation Center of Advanced Microstructures, Nanjing University, No.22 Hankou Road, Nanjing, 210093, Jiangsu, China.

*Corresponding author(s). E-mail(s): zhangyong@nju.edu.cn;
Contributing authors: xczphysics@gmail.com;

Abstract

To find a suitable incubator for nonlinear crystal optics(NCO), we have revisited linear crystal optics(LCO). At the methodological level, three widely used plane wave bases are compared in terms of eigenanalysis in reciprocal space and light field propagation in real space. Inspired by complex ray tracing, we expand M.V. Berry's 2003 uniform plane wave model to non-uniform Fourier crystal optics(FCO) and ultimately derive the explicit form of its 3×2 transition matrix, bridging the two major branches of crystal optics(CO) in reciprocal space, where either ray direction \vec{k} or spatial frequency \vec{k}_ρ serves as the input variable. Using this model, we create the material-matrix tetrahedral compass(M-M TC) to conduct a detailed analysis of how the four fundamental characteristics of materials (linear/circular birefringence/dichroism) influence the eigensystems of the vector electric field in two-dimensional(2D) spatial frequency \vec{k}_ρ domain and its distribution in three-dimensional(3D) \vec{r} space with a crystal-2f system. Along this journey, we have uncovered new territories in LCO in both real and reciprocal space, such as infinite singularities arranged in disk-, ring-, and crescent-like shapes, "L shorelines" resembling hearts, generalized haunting theorem, double conical refraction, and optical knots it induces. We also present our model's early applications in focal engineering and NCO.

Keywords: Crystal optics, Singular optics, Wave optics, Fourier optics, Nonlinear optics, Angular spectrum theory, Anisotropic diffraction, Plane wave model, Vector field, Maxwell equation, Partial differential equation, Constitutive relations, Boundary conditions, Generalized Snell's law, Eigenanalysis, Characteristic equation

Contents

1	Introduction	2
2	Results	5
2.1	Uniform plane waves to non-uniform Fourier optics	5
2.2	Eigensystems in 2D reciprocal space	6
2.3	Propagation in 3D real space	10
2.4	Tightly focused light in highly anisotropic materials	14
2.5	Superstructure of this model: nonlinear crystal optics	16
3	Discussion	18
4	Methods	19
4.1	Boundary conditions for laboratory settings	19
4.2	Eigensystem corrections for phase continuity	20
4.3	Overall flowchart of this model	22
4.4	Computational limitation 1 of this model	23
4.5	Computational limitation 2 of this model	25
4.6	Visualization for eigenvector field on 2D manifold	25
4.7	Visualization for vector electric fields on 2D manifolds	25

1 Introduction

Out of the 32 macroscopic crystal symmetries, 21 display non-centrosymmetry, enabling second harmonic generation(SHG) within these point groups. However, among these 21 crystal classes, 18 are birefringent or anisotropic, and more than half(11) exhibit natural optical rotation, demonstrating inherent optical activity(OA) or chirality[1]. As a result, nonlinear crystal optics(NCO) including second- or higher-order harmonics and other frequency-mixing phenomena, often encounter tremendous computational challenges[2, 3], due to the complexity of linear optical processes in low-symmetry materials, i.e. both pump/fundamental waves(FWs) and the newly generated frequencies(NFs) $\{\omega_i\}$ driven by them, must undergo independent (anisotropic) diffraction during subsequently linearly superposition, while potentially enduring absorption or gain within the crystal[4].

Beyond the anisotropy of the uniformly distributed complex tensor $\bar{\bar{\epsilon}}$ itself, the micro-nano structures modulated by fabrications on the material's $\bar{\bar{\epsilon}}(\mathbf{r})$ and $\bar{\bar{\chi}}^{(2)}(\mathbf{r})$ [5–8] tensors in recent engineering developments, likewise call for an immediate and precise consideration of the scattering and diffraction effects caused by the material's (sub)wavelength-scale inhomogeneity, both for FWs and NFs $\{\omega_i\}$ [9, 10]. Hence, from first principles, nonlinear crystal optics(NCO) is fundamentally built upon linear crystal optics(LCO). As such, a thorough mastery of LCO is a prerequisite before delving into NCO.

To lay a solid foundation for the subsequent analytical development of NCO, we have parallelly and systematically revisited the available approaches to achieving exact solutions of crystal optics(CO) from a top-down perspective: spanning from the exact solutions of vector NCO in bi-anisotropic materials all the way down to LCO well-known for its bi-quadratic characteristic equations (\supseteq Fresnel wave-normal equations), evaluating the equivalence, advantages and limitations of each method.

During this pilgrimage of revisiting LCO (see Supplementary Note 1), we find 4 problems, the last of which introduces the main topic of this paper:

(1) The matrix exponential(ME) $e^{i\bar{a}^\omega z}$, $e^{-i\bar{H}t/\hbar}$, as the most general form of the plane wave[11–14] and a promising approach for resolving field of degenerate eigenvectors on a large scale, represents the general solution for most linear systems. However, a universal and efficient numerical solution especially near the array of exceptional points(EPs) (i.e. singularities[15, 16]) remains elusive[13].

(2) Prolonged gain or even absorption over time or space, invariably leads to the divergence of ME[12], rendering ME unsuitable for addressing large-scale non-Hermitian systems.

(3) If the exponential/phase part of the ME is reduced to include only the eigenvalues, and the eigenvectors are moved out to multiply with the exponential term (i.e. $\bar{v}_i^\omega \cdot e^{i\lambda_i^\omega z}$ or $\bar{v}_i^{\omega T} \cdot e^{i\lambda_i^\omega z} \cdot \bar{v}_i^{\omega -T}$) — without being decomposed through Jordan Decomposition(JD) or equivalent methods[17, 18] — then the EPs can no longer be unfolded, and the underlying dynamics of field propagation and evolution will become completely uncomputable at that point.

(4) As the elementary form of the plane wave[17] and a simple eigensolution of the wave equation, $e^{i\bar{k}^\omega \cdot \bar{r}}$ provides an easily accessible orthonormal complete basis for reconstructing any complex scalar field $\in \mathbb{C}(\mathbb{R}^3)$ distributed in real space $\in \mathbb{R}^3$, and offers a vital tool for eigenanalysis in reciprocal space $\in \mathbb{R}^2$, sparking a highly productive exploration across various realms of physics for over 200 years[17, 19, 20].

However, regarding the input variable of the complex wavevector $\bar{k}^\omega \in \mathbb{C}^3$ in the phase $\bar{k}^\omega \cdot \bar{r}$ of the plane wave $e^{i\bar{k}^\omega \cdot \bar{r}}$, two different opinions

$$\bar{k}^\omega(\hat{k}) = k_0^\omega n^\omega(\hat{k})\hat{k} \in \mathbb{C}_r \times \mathbb{R}_\Theta^2 \subsetneq \mathbb{C}_\lambda^3, \quad (1a)$$

$$\bar{k}^\omega(\bar{k}_\rho) = \bar{k}_\rho + k_z^\omega(\bar{k}_\rho) \in \mathbb{R}_\perp^2 + \mathbb{C}_z, \quad (1b)$$

are held, where both $e^{ik_0^\omega n^\omega \hat{k} \cdot \bar{r}}$ and $e^{i(\bar{k}_\rho \cdot \bar{\rho} + k_z^\omega z)}$ satisfy the same wave equation.

More specifically, in terms of LCO, by substituting $\bar{E}^\omega(\bar{r}) = \bar{g}^\omega \cdot e^{i\bar{k}^\omega \cdot \bar{r}}$ into the wave equation for the electric field $\bar{E}^\omega(\bar{r})$ in a electrical anisotropic dielectric (see

Supplementary Note 2), it becomes evident that both plane wave expressions $\bar{g}^\omega(\hat{k}) \cdot e^{ik^\omega(\hat{k})\hat{k}\cdot\bar{r}}$ and $\bar{g}^\omega(\bar{k}_\rho) \cdot e^{i\bar{k}^\omega(\bar{k}_\rho)\cdot\bar{r}}$ share the same 3D characteristic equation

$$(k_\omega^2 - \bar{k}^\omega \bar{k}_\omega^\top - k_{0\omega}^2 \bar{\bar{\epsilon}}_{rz}^\omega) \cdot \bar{g}^\omega = \bar{0}. \quad (2) \quad 5 \mid 4, 6, 6, 18, 23.$$

From the perspective of simplicity, $\bar{g}^\omega(\hat{k}) \cdot e^{ik^\omega(\hat{k})\hat{k}\cdot\bar{r}}$ is superior to $\bar{g}^\omega(\bar{k}_\rho) \cdot e^{i\bar{k}^\omega(\bar{k}_\rho)\cdot\bar{r}}$. If the complex vector fields $\bar{k}^\omega, \bar{g}^\omega$ are expressed in terms of spatial frequency $\bar{k}_\rho \in \mathbb{R}_\perp^2$ in 3D Cartesian coordinate system (λ), it is typically necessary to numerically solve quartic equations for k_z^ω in order to obtain the eigenmodes of the electric field. On the other hand, if the input variables are expressed as uni-directions $\hat{k} \in \mathbb{R}_\ominus^2$ in real spherical coordinates (\ominus), Eq. (2) can always be reduced to the form of a bi-quadratic equation, which therefore has a closed-form solution for uniform plane waves in unbounded media, regardless of the material's complex $\bar{\bar{\epsilon}}_r^\omega$ tensor.

However, in terms of accuracy, $\bar{g}^\omega(\bar{k}_\rho) \cdot e^{i\bar{k}^\omega(\bar{k}_\rho)\cdot\bar{r}}$ is superior to $\bar{g}^\omega(\hat{k}) \cdot e^{ik^\omega(\hat{k})\hat{k}\cdot\bar{r}}$. Eigenmode in the form of $\bar{g}^\omega(\bar{k}_\rho) \cdot e^{i\bar{k}^\omega(\bar{k}_\rho)\cdot\bar{r}}$ naturally satisfies the requirements of Fourier transform(FT) and phase continuity boundary conditions, while $\bar{g}^\omega(\hat{k}) \cdot e^{ik^\omega(\hat{k})\hat{k}\cdot\bar{r}}$ fails to automatically meet these two requirements, especially when the material exhibits absorption or gain (see Methods).

In this work, we present a simple and practical approach to balance the advantages and disadvantages of these two mainstream models in the field of LCO, resulting in the 3×2 transition matrix for non-uniform[18, 21, 22] linear Fourier[23] crystal optics(LFCO), as shown in Fig. 1. Next, we introduce the ‘material-matrix’(M-M) tetrahedron compass (TC) in Fig. 2, where scanning parameters along three of its edges depict a theoretical panorama of the adiabatic evolution(AE) of electric field eigenmodes in the \bar{k}_ρ domain, competing among the three primary material properties, i.e. linear dichroism(LD), circular dichroism(CD), and optical activity(OA). During this process, we observe that CD, adhering to the haunting theorem as well, can lead to heart-shaped L shorelines and an infinite array of singularities in 2D \bar{k}_ρ domain, often arranged in patterns resembling disks, rings[24], or crescents.

Aided by crystal-2f system, we map out a second, more experimentally relevant panorama in the 3D \bar{r} domain in Figs. 3 and 4, freezing the AE of the light field distribution between the three vertices of the M-M TC (corresponding to the material's biaxiality(Bi), LD, and OA). Furthermore, we offer a unified solution for the forward propagation and inverse design of focal fields under high numerical aperture(N.A.) in Fig. 7. Along the way, we have observed two surprising phenomena: double conical refraction(DCR) and the resulting optical field knots. Finally, we offer a roadmap for expanding this LCO model in Fig. 8, demonstrating its applications in vector nonlinear Fourier crystal optics(NFCO) through full conical phase matching and chiral second harmonic conical refraction(SHCR).

2 Results

2.1 Uniform plane waves to non-uniform Fourier optics

In order to directly utilize the closed-form solutions $n^\omega(\hat{k})$ to the bi-quadratics from existing models, we express the independent variable \hat{k} as a function of \bar{k}_ρ as follows

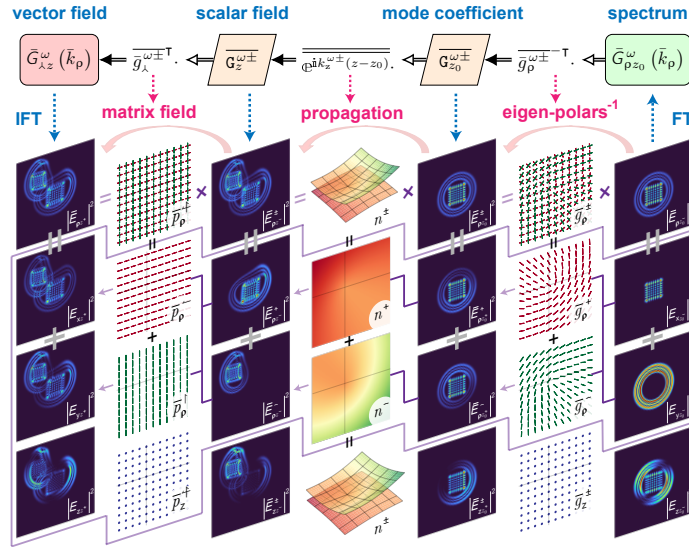
$$\hat{k}(\bar{k}_\rho) = \mathcal{N} \left\{ \text{Re} \left[\left(\bar{k}_\rho, \sqrt{k_{0\omega}^2 n_\omega^2(\hat{k}) - k_\rho^2} \right)^\top \right] \right\}, \quad (3) \quad 2 \mid 5, 5.$$

which is a transcendental equation of \hat{k} with $n_\omega^2(\hat{k})$ being provided by various even-spectrum models[1, 15, 16, 25–32]. Eq. (3) can be solved through direct iteration (see Method), Newton’s iteration[33], or other methods (see Section 2.4 and Discussion), with convergence typically occurring within two iterations when anisotropy is weak and the N.A. is small.

The eigenvalues and eigenvectors of non-uniform LFCO can be obtained by respectively substituting \hat{k} obtained through Eq. (3) into

$$k_z^\omega(\hat{k}) = \sqrt{k_{0\omega}^2 n_\omega^2(\hat{k}) - k_\rho^2} \quad (4)$$

and $\bar{g}^\omega(\hat{k})$ in Method. Then, as depicted in Fig. 1 and Method, the eigenvalue



Quoted @ 9 pp.
4, 5, 6, 22, 22,
22, 23, 23, 26.

Fig. 1 The core procedure for computing the optical vector fields between any two sections within an arbitrary $\bar{\epsilon}$ material, i.e., sequentially left-multiplying three eigensystem matrix fields. Below the first row, an example is provided for calculating the x, y, z components of the output vector optical field distribution (in the leftmost column). Initial condition: the known x, y components of the input 1064 nm pump (from the rightmost column), incident normally on the 15-mm-long KTP crystal with a 2° deviation off its optical axis. The vector pump is composed of vertically polarized $\text{LG}_{l=50}^{p=2}$ and horizontally polarized $\text{HG}_{6,6}$.

pairs $k_z^{\omega\pm}$ construct the propagation matrix $\overline{\overline{e^{ik_z^{\omega\pm}(z-z_0)}}}_{[2\times 2]}$, while the eigenvector pairs $\bar{g}^{\omega\pm}$ form the polarization state matrices $\overline{\overline{g_\lambda^{\omega\pm}{}^\top}}_{[3\times 2]}$ and $\overline{\overline{g_\rho^{\omega\pm}{}^{-\top}}}_{[2\times 2]}$. A sandwich multiplication of these three matrices yields the 3×2 transition matrix

$$\bar{T}_{\lambda z \rho}^\omega = \overline{\overline{g_\lambda^{\omega\pm}{}^\top}} \cdot \overline{\overline{e^{ik_z^{\omega\pm}(z-z_0)}}} \cdot \overline{\overline{g_\rho^{\omega\pm}{}^{-\top}}} \quad (5a)$$

$$= \begin{pmatrix} g_x^{\omega+} & g_x^{\omega-} \\ g_y^{\omega+} & g_y^{\omega-} \\ g_z^{\omega+} & g_z^{\omega-} \end{pmatrix} \cdot \begin{pmatrix} e^{ik_z^{\omega+}(z-z_0)} & 0 \\ 0 & e^{ik_z^{\omega-}(z-z_0)} \end{pmatrix} \cdot \begin{pmatrix} g_x^{\omega+} & g_x^{\omega-} \\ g_y^{\omega+} & g_y^{\omega-} \end{pmatrix}^{-1}. \quad (5b)$$

which realizes the transition $\bar{G}_{\rho z_0}^\omega \rightarrow \bar{G}_{\lambda z}^\omega$ from the two-component vector field $\bar{G}_\rho^\omega = (G_x^\omega, G_y^\omega)^\top$ on the input plane at z_0 to the three-component vector field $\bar{G}_\lambda^\omega = (G_x^\omega, G_y^\omega, G_z^\omega)^\top$ on the output plane at z through $\bar{G}_{\lambda z}^\omega = \bar{T}_{\lambda z \rho}^\omega \cdot \bar{G}_{\rho z_0}^\omega$. Coupled with FT pairs $\mathcal{F}[\bar{E}_\lambda^\omega(\bar{\rho})] = \bar{G}_\lambda^\omega(\bar{k}_\rho)$, Eq. (5) allows us to study the evolution and 3D distribution $\bar{E}_{\lambda z}^\omega(\bar{\rho}) = \bar{E}_\lambda^\omega(\bar{r})$ of the vector electric field $\bar{E}_\lambda^\omega = (E_x^\omega, E_y^\omega, E_z^\omega)^\top$ in arbitrary anisotropic dielectrics in real \bar{r} space, as demonstrated in Fig. 1.

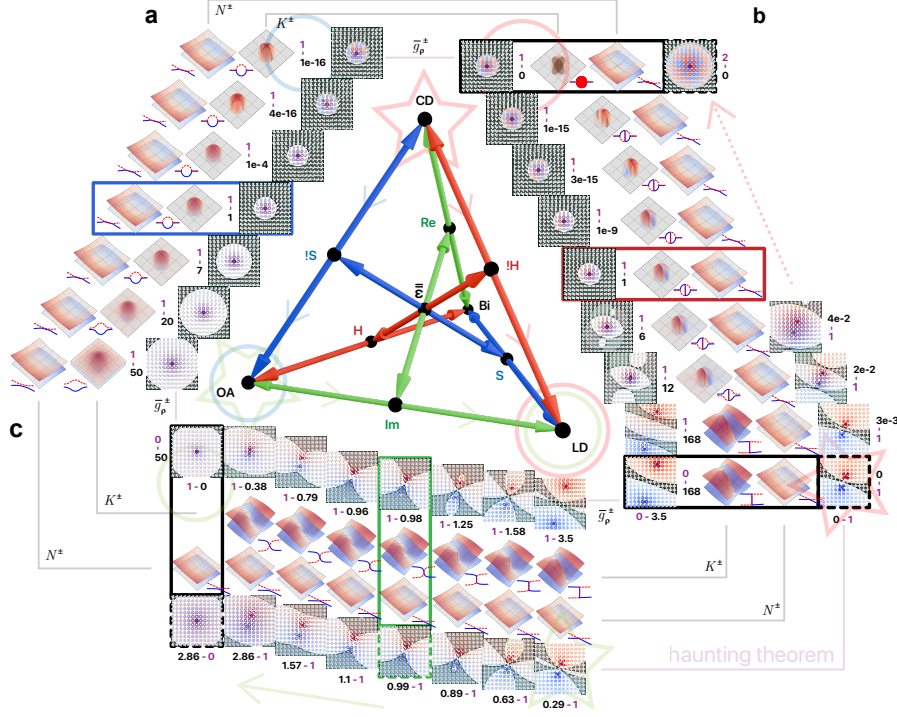
2.2 Eigensystems in 2D reciprocal space

Arbitrary complex dielectric tensors $\bar{\bar{\epsilon}}_r^\omega$ are typically associated with biaxial-chirality-absorption dielectrics. In order to relate the mathematical properties of the $\bar{\bar{\epsilon}}$ matrix to the optical/physical properties of the material, we propose the M-M TC in Fig. 2. The M-M TC consists of 6 edges: Hermitian(H), non-Hermitian(!H), symmetric(S), antisymmetric(!S), real part(Re), and imaginary part(Im) — corresponding to the six mathematical attributes of a complex matrix ($\bar{\bar{\epsilon}}$). The M-M TC consists of 4 vertices: biaxiality(Bi), optical activity(OA), linear dichroism(LD), and circular dichroism(CD) — describing the four optical properties of matter.

LCO then begins with the eigensystems of Eq. (2). The potentially complex $\bar{\bar{\epsilon}}_r^\omega$ in Eq. (2) is generally non-diagonalizable in 7 out of 11 cases, unless $\bar{\bar{\epsilon}}_r^\omega$ is a normal matrix, corresponding to the 4 possible combinations, that is, OA + Bi, LD + CD, Bi + LD, OA + CD, i.e. two endpoints of the 4 edges ‘H’, ‘!H’, ‘S’, ‘!S’, respectively. With the help of the M-M TC, we begin to explore the pairwise competition between CD, OA, and LD, and how it affects the AE of the eigensystem pairs’ distribution.

Let us start from the outermost circle of the three complete inner circles in Fig. 2, which represents the effective refractive indices’ real parts $N^{\omega\pm}$ (defined by Eq. (S20a) in Supplementary Note 2.2), followed by their imaginary parts $K^{\omega\pm}$, and then the eigen-polarization states $\bar{g}_\rho^{\omega\pm}$, arranged from the outer round to the innermost. For full AE process of these three circles, see Supplementary Video 1.

The ‘!S’ edge of the M-M TC in Fig. 2a shows the case when OA increases from 0 at the vertex ‘CD’ to the maximum at ‘OA’ (guided by the inner light blue arrows). The real and imaginary part of the effective eigenvalue-pair sheets N^\pm, K^\pm will first separate from a initial adherence around optical axis(o-a) within a constant-radius singularity disk during $OA < CD$. When OA reaches CD, solid singularity disk totally disintegrates from within, forming a hollow singularity ring. After $OA > CD$, adherences = singularities = degeneracies dissolve, and both the N^\pm, K^\pm sheets evolve into



Quoted @ 15 pp.
 4, 6, 6, 6, 8, 8, 9,
 9, 9, 9, 9, 9, 9, 9,
 9.

Fig. 2 Scan OA, LD, and CD along 3 edges ('!S', '!H', and '!Im') of the M-M TC to see the AE of eigensystems in 2D reciprocal k_p space. In the pairwise competition between OA, LD, and CD, one remains fixed, as reflected by the magenta number 1 in the proportional scale. The colors of polarization ellipses, C points (smaller circles) and singularities (solid dots), map to ellipticity $e = \tan(\chi) = b/a$, where red/blue correspond to right-/left-handed chirality, $-/+$ spin quantum number σ , as well as $+/-$ ellipticity, respectively. The eigenvector ellipses and the L shorelines, both depicted with dashed/solid lines, represent the slow/fast= s/f modes, corresponding to the upper/lower eigenvalue $N^{\omega\pm}$ sheets of $-/+$ modes. **a** By maintaining a fixed CD, increase OA incrementally from 0 to analyze how the CD-OA competition influences the eigensystems. **b** With CD (3 columns from the left) or LD (rightmost column) held constant, progressively raise LD or CD starting from 0 to observe the effects of CD-LD competition. **c** While keeping OA (3 rows from the top) or LD (bottom row) constant, gradually increase LD or OA from 0 to examine the impact of the OA-LD competition on the eigensystems.

two mirror-symmetric wide-brim Mexican sombreros, where the crowns of the N^\pm sheets are flatter, and the brims are more curled; conversely, the K^\pm sheets' brims are completely level, and its crown are more convex[24]. As OA increases from 0, the separation order of the paired N^\pm, K^\pm sheets is as follows: from the center of the disk to the outer edge/ring \rightarrow along the ring $\rightarrow N^\pm, K^\pm$ overall, throughout which the absolute height of the two sombreros of K^\pm almost stays constant and is nearly solely determined by CD, with little relevance to OA.

Considering the corresponding AE of the eigenvectors' distribution. When OA = 0, an infinite number of optical singularities exist within the disk, with the eigenvectors inside being pairwise degenerate into random left-handed or right-handed elliptical polarization(R/LHEP), whose ellipticity's magnitude $|e|$ decreases from the

center(o-a) to the periphery. As OA increases, the singularities within the disk gradually dissipate in a cross-shaped pattern, eventually vanishing entirely when OA reaches CD. At this point, the four remaining degenerate sectorial areas of the “pizza disk” also disappear, leaving behind a ring of singularities, which serves as the criterion for the condition $CD = OA$. When OA starts to exceed CD, the ring-like singularities begin to dissipate randomly and sporadically. Once the singularity ring fully dissipated, the threshold ring of near linearly polarized(LP) eigenvectors corresponding to $|e|_{\min} + 20\%(\langle |e| \rangle - |e|_{\min})$ ¹ =: “L shorelines” which almost coincides with it starts to expand, until it reaches its maximum along with OA.

Along the ‘Im’ edge of the M-M TC in Fig. 2c, as LD increases from 0 at the vertex ‘OA’ to the maximum at ‘LD’ (indicated by the inner light green arrows), the paired N^\pm sheets transition from a separated state to “line contact”, creating a half-trench depression within the originally higher N^- , dipping below the lower N^+ . One side of the trench gradually descends beneath N^+ , while the other side abruptly ascends and surpasses N^+ once more. In contrast, the peak of N^+ behaves oppositely: one side rises steadily above N^- , and the other side sharply drops below it. Excluding the discontinuity at the step cliff, N^\pm sheets together create a continuous intersecting manifold, with their half-peak/trench interlocked, forming a hollow Mexican roll. In the case of K^\pm sheets that permanently intersect, the shared cliff caused by LD can be directly described using two opposite step-like functions that share the same zero point. The altitude of the cliff fault for each mode is determined by the limits at its two ends, which extend in opposite directions away from the optical axis. This altitude is almost entirely governed by LD itself, with minimal dependence on OA, similar to the case where OA versus CD in Fig. 2a. Under the additional effect of OA, the section of the cliff resembles function arctan, sigmoid, or tanh; whereas competing with CD, the mirror-image cliffs form a pair of C2-symmetric Z-buckles.

Correspondingly, in terms of the eigenvectors, the gray/green background layers, also referred as “L lakes”, enclosed by the dashed/solid L shorelines, outline the regions where the eigenpolar of the $-/+$ modes approach LP, serving as a substitute for L lines[15]. When $LD = 0$, both the C points and the L shorelines of the two \pm modes fully overlap, with the \pm L lakes coinciding to form a deep green color. As LD increases, the L shorelines and the paired C points with opposite handedness (which belongs to different \pm modes respectively) no longer coincide. The C points move away from the o-a, and the L shorelines resembling magnetohydrodynamics, are attracted by o-a in the direction aligning with the motion of their own C points. When $OA = LD$, the two L shorelines meet at the o-a, forming the first 8-shaped ring perpendicular to the line connecting the C points(C-C). At this stage, the paired singularities, acting as (ultimately) degenerate eigenvectors of the Voigt wave, emerge at the o-a. As LD continues to exceed OA, another pair of C points and singularities emerge, and a second 8-shaped ring appears along the direction away from the o-a, parallel to the C-C. Finally, when LD reaches its maximum and $OA = 0$, the first 8-shaped ring perpendicular to the C-C disappears. Concurrently, the \pm L lakes overlap once more, partitioning the remaining second 8-shaped ring like the Chu-Han Contention.

¹ $\langle |e| \rangle$ represents the average value of $|e|$.

Along the ‘!H’ edge of the M-M TC in Fig. 2b, as LD increases from 0 at the vertex ‘CD’ to the maximum at ‘LD’ (depicted by the inner light red arrows), during the first half of the process where $LD \leq CD$, the behavior of the eigenvalues for the N^\pm, K^\pm sheets mirrors that observed in Fig. 2a, where OA is increased from 0 in the presence of CD along ‘!S’ edge. The only difference is that the left half of N^\pm, K^\pm (which is cut by LD) is flipped upside down, i.e. swaps their respective values within the ring of singularities, which symbolizes the balance where $LD = CD$. During the second half, dominated by LD, both sides of the two K^\pm , the left side of lower N^+ and the right side of upper N^- , are ironed horizontally, while the right side of N^+ and the left side of N^- are straightened at an angle, identical to that of the conical refraction(CR). The absolute elevation of the cliff/Z-buckle in K^\pm caused by LD and OA, different from the distance between the two peaks of the crowns of K^\pm in Fig. 2a, is changing during variations in LD, thus is not entirely determined by CD.

Correspondingly, the AE of the eigenvectors turns out to be unexpectedly interesting. As LD gradually increases from 0, competing with constant CD, the first half of the ‘!H’ edge remains similar to the ‘!S’ edge of Fig. 2a. When $LD \gtrsim CD$, the singularity ring is torn apart by LD, with the remaining crescent singularities aligning in the upcoming C-C direction. Afterward, when LD surpasses CD, the mirror-symmetric L shorelines of the two \pm modes, both featuring double center-symmetric half- π helical lines, start to expand overall like a heart-shaped pendant adorned with hollow water droplets. And the paired C points move towards the remaining singularities and eventually surpass their original positions. Throughout this process, the two ends of the incomplete crescents of singularities, controlled solely by CD, remain fixed. Before the C points arrive, the ring dissipates to leave only one pair of singularities (rather than infinite ones) as the ordinary case in classical LCO. As LD increases further, the singularities move in the same direction as the C points, but at a slower speed, until they eventually meet and coincide, at which point LD reaches its maximum and CD drops to zero. During the attenuation of CD, the split L lakes of same mode begin to move inward from both sides toward the o-a, ultimately merging into a single strip of the same color (green or gray), controlled solely by LD. Throughout this process, if LD remains unchanged, the absolute position of the C points will also remain constant (as per the haunting theorem[15]), and the singularities will retract to the positions of the C points.

For the outermost 4th incomplete circle formed by eigenvectors, we merely present it to generalize the haunting theorem. Under the condition of a constant LD, the haunting theorem applies not only to the varying OA (Fig. 2c), but also to the varying CD (Fig. 2b). See Supplementary Video 2 for further details. Regarding the missing portions of the outermost circle in Fig. 2, the corresponding phenomena are either too trivial (Fig. 2a), or exceed the region of interest(ROI) (Fig. 2b).

CD, as the real and anti-symmetric part of the $\bar{\bar{\epsilon}}_r^{\prime\omega}$ tensor, along with its impact on modes’ eigensystems and light propagation, has been additionally emphasized during our expedition this time, based on the Born-Landau’s constitutive relations(CRs). As the asymmetric counterpart to the Drude Boys’ (Post’s) CRs, Born Landau’s CRs are largely applicable, but they are not strictly correct[1, 34]. This limitation manifests in two ways: the infinite singularities introduced by CD in reciprocal space, and the

violations of physical realism observed during real-space propagation. In particular, under the Born Landau's CRs, CD — usually acting as the antisymmetric part of a real matrix — typically produces paired complex conjugate eigenvalues. Consequently, of the two eigenmodes along the propagation direction, one exhibits absorption while the other shows gain, with their combined energy almost invariably exhibiting net gain during propagation in numerical simulations. This contradicts the experimental observation that CD, akin to LD, should exhibit absorption in both \pm modes[35], although the always accompanied isotropic loss might offer an explanation. Consequently, a thorough and focused study of CD within symmetric CRs in bianisotropic materials becomes imperative.

2.3 Propagation in 3D real space

We highlight the superiority of the crystal-2f configuration in numerical experiments

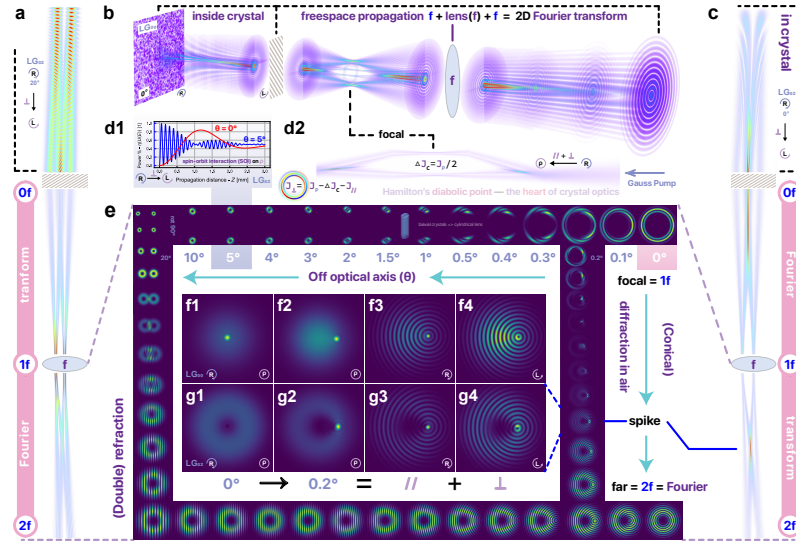


Fig. 3 The adiabatic transition from DR (a and the left column of e) to CR (c and the rightmost column of e) as the pump deviates/approaches the diabolical point, focusing on the focal-plane (top row of e) and far-field (bottom row of e) evolution, as well as the full-field propagation of DR (a) and CR (b, d, and c), all of which are investigated by a standard crystal-2f system. a,c The full-field 2D evolution of the left-handed circular polarization(LHCP) component of a right-handed circularly polarized(RHCP) $LG_{l=2}^{p=0}$ mode pumped at 20° (a) or 0° (c) off the o-a, double refracting (a) or conical diffracting (c) inside and outside the KTP crystal. b the 3D version of c with the pump replaced by a Gaussian beam, and the focal plane situated between the crystal's rear surface and the lens. d1 Transverse R \rightarrow L SOI efficiency evolution inside KTP when the $LG_{l=2}^{p=0}$ pump is aligned off-axis at 0° and 5° , respectively. d2 the 2D, analyzer-free version of b in the context of classical CR, where the pump loses half of its total angular momentum J_P , which is transferred to the crystal. e An extended study based on Peet's experimental results, where (f1-f4) and (g1-g4) correspond to Figures 7(a-h) in Peet's work[36], surrounding which the pump-o-a angle is scanned horizontally from 0° to 20° , while the propagation distance is scanned vertically from the focal plane at $z = f$ to the Fourier far field at $z = 2f$, with the off-axis Raman spike emerges somewhere in between $(f, 2f)$. The four edges are connected end-to-end, forming an AE band in 3D real \vec{r} space under another set of parameters θ, z .

Quoted @ 6 pp.
4, 11, 11, 11, 12,
12.

in 3D real \bar{r} space by detailing the AE from double refraction(DR) off the o-a to CR along the o-a in Fig. 3. Here, the pump-CCD is set under R-L(Right-Left circular) polarizer-analyzer configuration in most cases, in order to analyze transverse R \rightarrow L spin-orbit interaction(SOI) inside crystal. The entirety of Fig. 3 can be regarded as the “analytical continuation” of Peet’s 2014 work[36] across two dimensions, i.e. the propagation distance z and the off-o-a angle θ .

We now revisit the M-M TC, upon completing the quantitative validation in Fig. 3 around the o-a, i.e. the diabolic point of a typical biaxial material, where the eigenvalue degeneracy does not extend to the eigenvectors. Along its three edges, namely

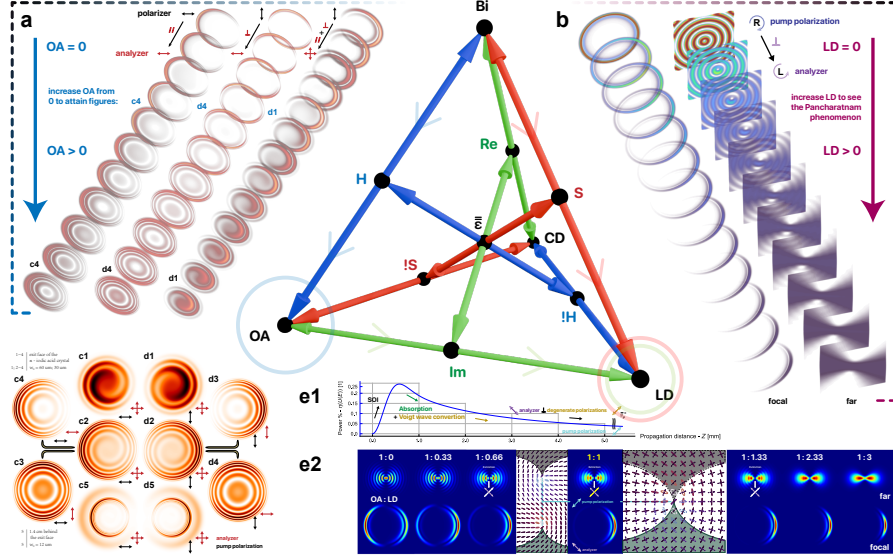


Fig. 4 Scan Bi, OA, and LD along 3 edges (‘H’, ‘S’, and ‘Im’) of the M-M TC to see the AE of optical fields in the 3D real \bar{r} space. **a** Increase OA to see chiral CR evolution at the focal plane, which ultimately results in (c1-c5) and (d1-d5), matching bloembergen’s experiment[37] in his FIG. 5A-9A and 5B-9B respectively. **b** Increase LD to see Pancharatnam phenomenon[38] and Brenier’s anisotropic absorbing spectrum[32, 39] (in his Fig. 6b). **e1** By Increasing LD while keeping OA constant, the competition between LD and OA is examined, providing extinction in the far field as the experimental criterion[40] for OA = LD under the setup where the pump’s polarization \parallel eigenvectors \perp analyzer. **e2** The corresponding evolution of H \rightarrow V SOI efficiency when OA = LD.

‘H’, ‘S’, and ‘Im’, we broadly reproduce experimental results of Pancharatnam[38], Bloembergen[37], Brenier[32, 39, 40] et al.[32, 37–44] in 3D real space, focusing on three optical properties of matter, i.e. Bi, OA, and LD.

Perform a counterclockwise scan along the three edges of the M-M TC. First, increasing OA from 0 along the ‘H’ edge of the M-M TC yields the AE diagram of the optical rotation field from vertex ‘Bi’ to ‘OA’ in Fig. 4e (pointed by the light blue arrows), ultimately converging to Bloembergen’s experiment: chiral CR[37] through α -HIO₃. Next, while maintaining OA, as LD increases along the ‘Im’ edge from 0 (denoted by the light green arrows), Brenier’s experimental results on chirality versus dichroism[40] of acentric chiral Nd³⁺-doped BZBO are obtained, with a clear criterion

Quoted @ 3 pp.
4, 11, 22.

for $OA = LD$. That is, when pump's polarization is aligned parallel to the polarization of Voigt wave while the analyzer is set perpendicular, central extinction is observed in the far field. Following this, by canceling OA and keeping only LD , the angular absorption distribution of laser crystal $KGd(WO_4)_2$ is obtained[32, 39]. Then, by gradually reducing LD along the 'S' edge (antiparallel to the light red arrows), the Pancharatnam phenomenon[38] emerges. Finally, as LD is reduced to 0, only Bi remains, including uniaxiality (Fig. 5b and Fig. 6), biaxiality (Fig. 5a and Fig. 6b1), and their hyperbolic counterparts (Fig. 5a and b).

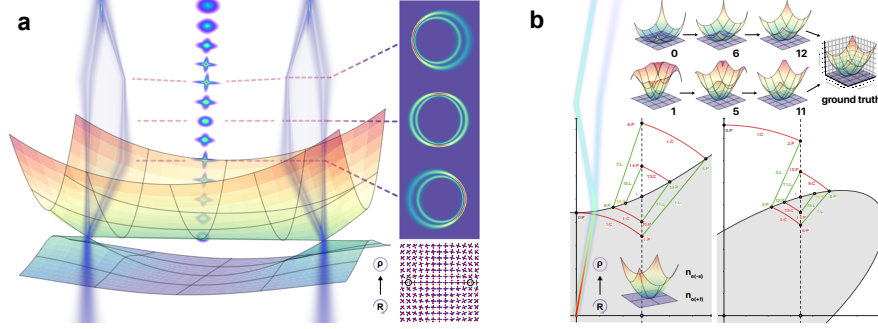
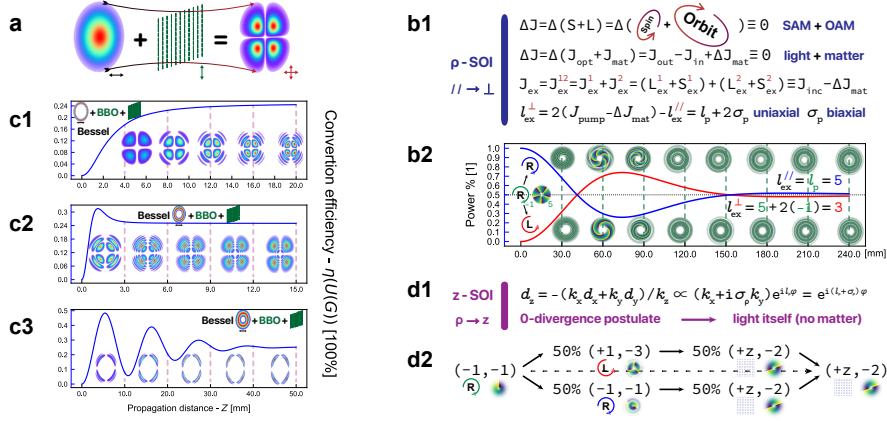


Fig. 5 The refractive index surfaces of hyperbolic materials and the corresponding energy flux profiles they modulate. a CR and cross beam propagating in hyperbolic biaxial materials[41]. **b** Negative refraction in hyperbolic uniaxial materials, and the iterative convergence of the highly anisotropic refractive index hyperboloid/ellipsoid.

Quoted @ 10 pp.
12, 12, 12, 12, 12,
12, 12, 12, 12, 25.

For the dielectric-type hyperbolic materials in Fig. 5a-b and Fig. 7d, typical phenomena such as double refraction(DR) in Fig. 5b, conical refraction(CR) in Fig. 5a, and double conical refraction(DCR) in Fig. 7d become nontrivial, all showing that the energy flow direction undergoes further modulation compared to ellipsoidal materials. This leads to effects such as the negative refraction of extraordinary rays and positive refraction of ordinary rays in Fig. 5b, cross-star diffraction in the middle of two optical axes in Fig. 5a, as well as the non-circularly symmetric (at the focal plane) or even non-c2-symmetric (away from the focal plane) CR patterns in Fig. 5a.

Using uniaxial materials in Fig. 6, we present the one-dimensional(1D) continuous evolution of typical (monotonic) and atypical (oscillatory) conversion efficiencies for horizontal→vertical(H→V) SOI in Fig. 6c and R→L SOI in Fig. 6b2. Correspondingly, we provide sliced sequences of the transverse optical field distribution at discrete propagation distances $\{z_i\}$. We observe that, apart from the high-frequency oscillation and its envelope caused by non-zero incident angles (blue line in Fig. 3d1), factors such as non-zero orbital angular momentum(OAM) of the pump (red line in Fig. 3d1 and Fig. 6b2), non-paraxiality in reciprocal space, and beam waist size in real space (Fig. 6c) also influence the shapes of the efficiency curves for H→V and R→L SOI. Interestingly, the H→V conversion efficiency for LP Bessel beams can reach as high as 50% (Fig. 6c3) under specific combinations of pump parameters and propagation distances, compared to the typical steady-state value of 25%. Additionally, in Fig. 6b1, we



Quoted @ 11 pp.
 12, 12, 12, 12,
 12, 12, 12, 12,
 12, 13, 13.

Fig. 6 Transverse (H-V, R-L) and longitudinal (ρ -z) SOI in uniaxial and biaxial materials. H \rightarrow V SOI and its efficiency evolution in (a) non-ideal analyzers[42] and (c) uniaxial crystals pumped by Bessel beams with different waist and cone. **b1** The conservation of total angular momentum $\Delta J = 0$ of light and matter leads to the explicit formula of transverse SOI in biaxial[43] and uniaxial crystals[44]; **d1** the divergence equation yields the explicit expression for the SOI in the z-direction. Illustrative explanations for both (**b2**) transverse and (**d2**) longitudinal SOI are also provided.

provide a simple derivation of the transverse SOI output topological charge l_{\perp} expressions in biaxial $l_{\perp} = \sigma_p$ and uniaxial materials $l_{\perp} = l_p + 2\sigma_p$ from the perspective of total angular momentum(TAM) conservation $\Delta J = 0$ in light-matter interaction. Furthermore, from the divergence equation, we derive a formula for predicting the topological charge l_z of the z-component electric field based on the transverse spin-orbit state of the pump σ_p, l_p in Fig. 6d1. Corresponding illustrative examples for both transverse and longitudinal SOI are provided in Fig. 6b2 and d2, respectively.

As an effect caused by the off-diagonal elements of the 2×2 eigen-polarization matrix $\overline{g}_{\rho}^{\omega \pm -T}$ and an embodiment of conservation law, the global grasp and detailed calculation of SOI play a significant role in not only LCO but also NCO[44].

2.4 Tightly focused light in highly anisotropic materials

In the extreme case of strong interaction between highly anisotropic materials and tightly focused light fields — an area at the forefront of both industry and academia in laser processing, aberration correction, and inverse focal engineering — our model

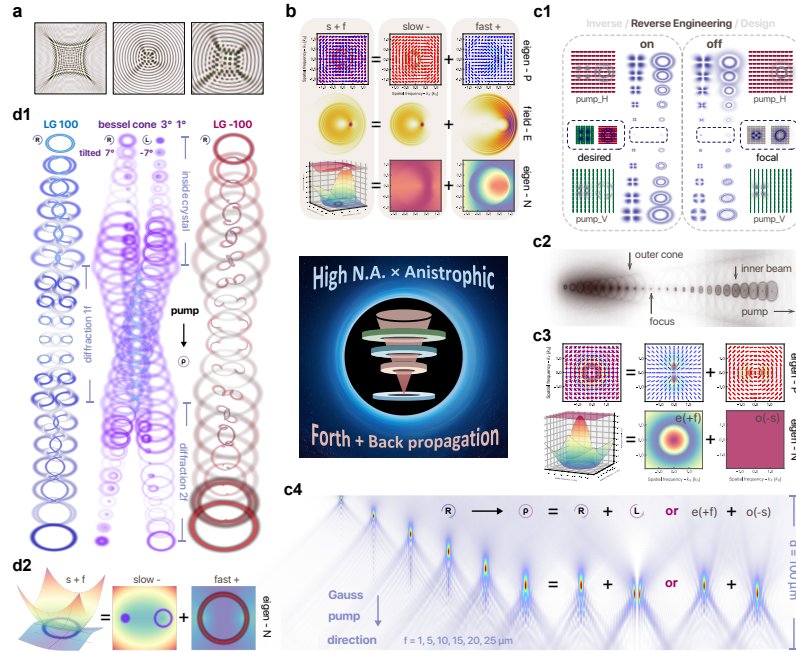


Fig. 7 Forward and backward propagation in anisotropic materials with high N.A. pump. **a** Bessel caustics reconstructed from Zusin et al. [45]. **b** Raman spike of CR origins solely from the slow mode. The vertically polarized off-o-a LG₁ pump is chosen to pump α -HIO₃. **c1** Inverse design of tightly focused focal fields: The backward propagation (BP) of the superposed \pm eigenmodes (left) eliminates the aberrations introduced by the direct isotropic BP (right) of the target desired vector field in the focal plane: horizontally polarized LG_{*l*=-10} [46] + vertically polarized HG₁₁, without the need for any Zernike polynomial compensation. **c2** In the case of high N.A., outside the axial field that first focuses and then diverges, a “Cherenkov cone” that continuously diverges exists independently. **c3** Lithium niobate (LN)’s eigensystems used to simulate (c1, c2, and c4), where vertically polarized Gaussian is used to simulate (c2). **c4** RHCP Gauss pump travels along the o-a of LN, with the objective aperture at the surface of the material. The first 6 spots from the left: By switching focal lengths, the intensity section distribution within the material at different depths without wavefront correction. Spots 7-10: Decomposing the sixth spot into L/RHCP or eigenmodes: respectively reveals the transverse SOI and the nature of axial multifocality when no aberration correction is applied — interference between mismatched o- and e-waves. **d1** A single light beam (left), or two coherent beams (middle), whose angular spectrum distributions in \vec{k}_ρ domain cover both optical axes of the (hyperbolic) biaxial crystal, undergo two separate conical refractions that superimpose and interfere. — In the case of a single beam, light field self-twisting behavior is likely to occur, especially when the reciprocal space coverage of the pump’s angular spectrum is greater than (right) or equal to (left) the angle of bi-axes. **d2** The distributions of the three pumps from (d1) in reciprocal space relative to the refractive index.

provides a unified solution, as shown in Fig. 7. Here, we show the origin of Raman spike (Fig. 7b), the reverse engineering technique for the targeted vector complex field at the focal plane free of Zernike polynomial (Fig. 7c1), the ‘‘Cherenkov cone’’ outside the inner beam (Fig. 7c2), the R-L and o-e decomposition analysis for high-N.A. pump (Fig. 7c4), and double conical refraction and the optical field self-twisting effects it induces (Fig. 7d1).

The interference of complex fields gives rise to the intricate and distorted shapes of light spots, especially in the case of tightly focusing. This phenomenon, emblematic of wave optics (paralleling quantum mechanics), as its most distinctive feature differentiating ray optics (analogous to classical mechanics), not only represents the mathematical frontier of highly oscillatory partial differential equations (PDEs), where both the inner integrand and the integral outcome are potentially highly oscillatory [47], but also pushes the computational limits in raising the speed-accuracy product under the constraints of the sampling theorem [48], thus stands as one of the most promising candidates for fully challenging the performance of all neural networks claiming that they are physical [49].

The strong anisotropy of the material further heightens the computational demands for calculating the light field distribution. This arises from the enhanced distortion of the electromagnetic field’s eigenvalue surfaces and their associated wavefronts (equiphase surfaces), compounded by the faster variation of eigenvectors controlling polarization directions which ultimately implement interference along x, y, z axes, hastening the premature arrival of the nightmare where phase differences exceeding π between adjacent pixels [50, 51] on a typical planar interference pattern at $z = z_0$.

Using the crystal-version vector angular spectrum method (ASM) without any optimization, we explored various tightly focused field distributions while operating at the edge of the sampling theorem, with each subfigure (except Fig. 7c2) in Fig. 7 nearing the computational limits just before aliasing errors occur. Initially, we believed that the origin of the outer cone in Fig. 7c2 was physical because: (1) it began forming even before propagation, and (2) it appeared at the center of the image rather than being reflected from the edges. However, we later discovered that it was still caused by aliasing errors originating from circular convolution. This conclusion was drawn because, in order to shift the focal plane of Fig. 7c2 inside the LN material, we set the incident field distribution at the material’s entrance to a LP Gaussian beam with a N.A. close to 1 (see the top row of Fig. 7c3), propagating backward by $z_0 = -0.2$ mm. However, when z_0 was set to zero, the outer ring disappeared. In contrast, Fig. 7c4 uses the transfer function of the objective lens instead of backward propagation to shift the focal plane below the upper surface of LN, completely eliminating the aliasing error.

We find that by setting ε_{zz} negative, thereby transforming the refractive index surface from an ellipsoid to a dielectric-type two-sheet hyperboloid, the two optical axes can be brought closer together, as shown in Fig. 7d2. For KTP crystal at 1064 nm, the angle between the two optical axes decreases from $34.6^\circ \times 2$ in the ellipsoidal case to $7.7^\circ \times 2$ in the hyperboloidal case, allowing us to compute the full evolution inside and outside the crystal in a non-paraxial manner over relatively longer propagation distances of the entire crystal-2f system. Optical field knotting in the 1st and 3rd

column of Fig. 7d1 are beyond our present mathematical understanding and techniques for explanation.

2.5 Superstructure of this model: nonlinear crystal optics

Nonlinear optics(NO), as a profound gateway for exploring and understanding light-matter interactions, introduces all higher-order nonlinear terms $\bar{P}_\omega^{(2)} + \bar{P}_\omega^{(3)} + \dots$ in the CRs beyond the first-order linear electric susceptibility $\bar{\chi}_\omega^{(1)} = \bar{\epsilon}_r^{\omega} - 1$. These

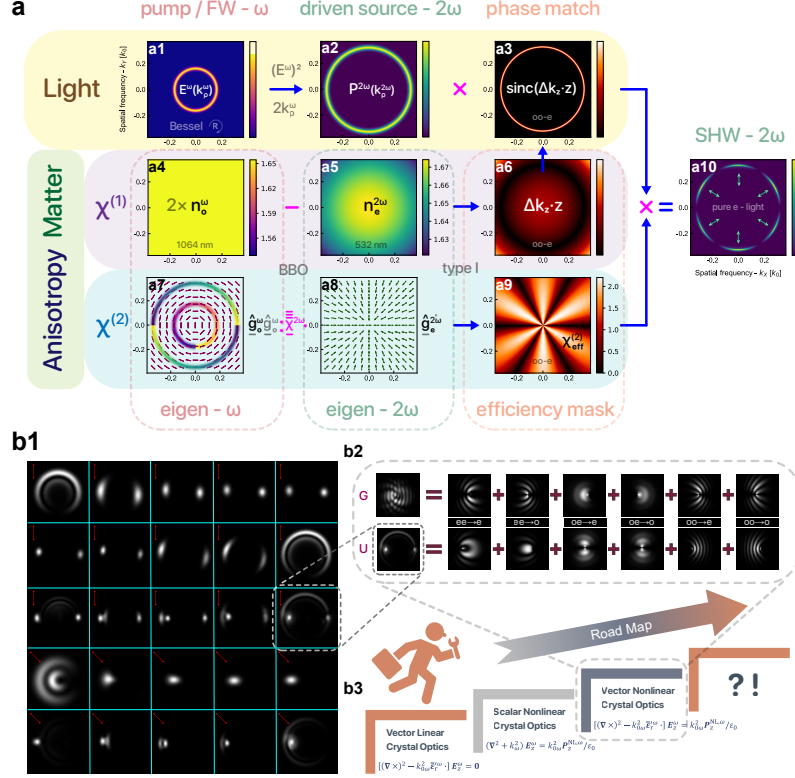


Fig. 8 Towards nonlinear Fourier crystal optics(NFCO). **a** Reinterpret type-I o+o→e full conical phase matching[52] along the o-a of BBO crystal for SHG within the framework of NFCO. On the first ‘light’ row, by squaring the RHCP Bessel FW (a1) and expanding its field of view with a twofold interpolation in the \bar{k}_ρ domain, the intracrystal nonlinear driven source $\bar{P}_{2\omega}^{(2)}$ (a2) is obtained. This traveling field, entirely determined by the pump, is multiplied by the “eigenvalue efficiency mask” = longitudinal phase matching coherence level (a3) derived from the path (a4→a5→a6→a3), followed by the “eigenvector efficiency mask” = effective nonlinear coefficient distribution[2, 3, 53, 54] (a9) from the path (a7→a8→a9). The resulting output in (a10) is a hexagonal conical radial vector light field purely composed of extraordinary light of BBO at 2ω . **b1** Reconstructed experiment results from Grant et al.[55] on Chiral SHCR by utilizing the third stage (in b3) of this LCO model: vector NFCO. **b2** The real-space and reciprocal-space distributions U, G of the 532 nm second harmonic wave(SHW) at the focal plane, generated by pumping a vertically polarized 1064 nm Gauss FW along the optical axis at 532 nm, along with its decomposition into six phase-matching types.

Quoted @ 12 pp.
4, 17, 17, 17, 17,
17, 17, 17, 17,
17, 17, 17.

higher-order terms represent the nonlinear response of bound electric dipoles to external optical fields. Ultimately, they act as cross-band light sources that coherently generate NFs within crystals through parametric radiation (there are also non-parametric/inelastic cases where phonons or molecules are involved[4]). Both the NFs $\{\omega_i\}$ and the pumps involved in the interaction, are constrained by their own monochromatic passive wave equation, necessitating independent diffraction as the crystal's eigenmodes (Fig. 8a4-5,a7-8). The parametric frequency conversion process must first satisfy energy conservation, followed by momentum conservation (often described as wave vector or phase matching), which further tests the precision of eigenvalue calculations (Fig. 8a4-5). If the anisotropy of the second-order nonlinear coefficient tensor $\bar{\bar{\chi}}_\omega^{(2)}$ is additionally involved, the accurate computation of eigenvectors (Fig. 8a7-8) in the \mathcal{C} frame[2, 3, 53, 54] within LCO must also be ensured as a prerequisite. These two core principles, i.e, passive independent diffraction and active coupled conversion of all $\{\omega_i\}$ that participate in nonlinear optical processes, anchor all nonlinear optical phenomena within the framework of LCO. The precise theoretical modeling of nonlinear processes in anisotropic materials becomes naturally, a more rigorous test for all established LCO models.

To showcase the basics of vector NFCO, Fig. 8a10 reproduces the full conical phase matching second harmonic generation(SHG) proposed by Belyi et al.[52], illustrating the calculation of $\omega \rightarrow 2\omega$ conversion in a uniaxial BBO crystal through Fig. 8a1-9, where both the first- and second-order susceptibilities $\bar{\bar{\chi}}_\omega^{(1)}, \bar{\bar{\chi}}_{2\omega}^{(1)}, \bar{\bar{\chi}}_{2\omega}^{(2)}$ are anisotropic.

In vector NFCO, transverse wave vector conservation (Fig. 8a1-2) is elevated to the same fundamental level as ω conservation and phase continuity at the boundaries, making it a prerequisite that must take priority. The conversion efficiency, determined solely by the longitudinal phase mismatch $\Delta k_z z$ (Fig. 8a6) and effective nonlinear coefficient (Fig. 8a9)[2, 3, 53, 54]

$$\chi_{3\text{eff}}^{(2)\text{P312}} := \hat{g}_{3\mu_3}^{\text{P3}*} \chi_{3\mu_3 12}^{(2)} \hat{g}_{1\mu_1}^{\text{P1}} \hat{g}_{2\mu_2}^{\text{P2}} =: \hat{g}_{\omega_3}^{\text{P3}*} \cdot \bar{\bar{\chi}}_{\omega_3}^{(2)} : \hat{g}_{\omega_1}^{\text{P1}} \hat{g}_{\omega_2}^{\text{P2}}, \quad (6) \quad 2 \mid 17, 17.$$

is subordinated to the fulfillment of transverse momentum conservation. Notably, p_1 , p_2 , and p_3 in Eq. (6) represents the eigen-polarization states \pm of ω_1 , ω_2 , and ω_3 in the \mathcal{C} frame, whose combination are fixed under certain phase-matching type. For example, phase-matching type-I $o+o \rightarrow e$ from Fig. 8a7-9 needs to compute $\hat{g}_{\omega_1}^{\text{P1}}, \hat{g}_{\omega_1}^{\text{P2}}, \hat{g}_{\omega_3}^{\text{P3}} = \hat{g}_\omega^o, \hat{g}_\omega^o, \hat{g}_{2\omega}^e$ from Eq. (6). Above eigenvectors in the \mathcal{C} frame are almost directly provided by Berry's 2003 model[15] in Fig. 9b, though a few minor adjustments in Fig. 9c are still required. This is why we have chosen to revisit and revise Berry's LCO model. It remains thoroughly classical in every aspect, from its CRs to its closed-form eigensystem induced by divergence equation, and its seamless integration into NCO.

As two masks determining the angular distribution of frequency conversion efficiency, the degree of longitudinal phase matching $\text{sinc}(\Delta k_z z)$ from Fig. 8a3 and the effective nonlinear coefficient $\chi_{2\omega;\text{eff}}^{(2)\text{ooe}}$ from Fig. 8a9, respectively, depend on the eigenvalues and eigenvectors in linear Fourier crystal optics(LFCO), reaffirming that NCO is fundamentally grounded in LCO, and both linear(LO) and nonlinear optics(CO) should ultimately be incorporated into the framework of Fourier optics(FO).

3 Discussion

In arbitrary $\bar{\epsilon}_r^{\prime\omega}$, namely biaxial-chiral-absorbing dielectrics, complex eigenmodes and their anisotropic diffraction behaviors form the fundamental basis of all advanced studies involving the interaction between light and matter. Of all the models created in an attempt to address this issue, the ultimate plane wave solution in the form of matrix exponential $e^{i\bar{a}^{\omega}z}$ after Jordan decomposition is regarded as the most likely key to deciphering the internal structure of singularities with second-order or higher degeneracy (see Supplementary Note). Yet, the numerical implementation of this approach is unstable and incapable of managing thicker non-Hermitian materials.

Conversely, numerically stable models that allow for the treatment of thick non-Hermitian slabs fail entirely to resolve EPs. These models share the same structure of classical plane wave $e^{i\bar{k}^{\omega}\cdot\bar{r}}$, whose two distinct forms $e^{ik^{\omega}(\hat{k})\cdot\bar{r}}$, $e^{i\bar{k}^{\omega}(\bar{k}_{\rho})\cdot\bar{r}}$ based on real spherical/rectangular coordinates, with different independent variables \hat{k} , \bar{k}_{ρ} , both satisfy the same wave/characteristic Eq. (2). All models choosing \bar{k}_{ρ} as input variable typically requires numerical solutions for quartics, while the rest models depends on \hat{k} possess simple closed-form solutions to biquadratics. However, the former satisfies FT and boundary conditions, while the latter does not.

In light of complex ray tracing, we extend M.V. Berry's 2003 uniform plane wave model to non-uniform LFCO and ultimately derive the explicit form of its 3×2 transition matrix field between any two sections within a planar slab dielectric, by transforming Berry's eigensystem $\hat{k}, \bar{d}^{\omega}(\hat{k})$ into $\bar{k}_{\rho}, \bar{g}^{\omega}(\bar{k}_{\rho})$, thus bridging the two major branches of crystal optics in reciprocal space, where either ray direction \hat{k} or spatial frequency \bar{k}_{ρ} serves as the input variable.

Using this model, we have comprehensively explored and revealed a new facet of the crystal optics from two perspectives: the AE of eigensystems in 2D reciprocal space under the dual competition among the four material properties: linear/circular birefringence/dichroism (via the material-matrix tetrahedron), together with the corresponding evolution of the light field in 3D real space (in collaboration with crystal-2f system), depicting two magnificent panoramic maps in both real and reciprocal space.

Along the way, we observe that circular dichroism(CD), which also conforms to the haunting theorem, can result in heart-formed L shorelines and infinite singularities arranged in disk-, ring-, and crescent-like shapes in 2D \bar{k}_{ρ} domain; while in 3D \bar{r} space, double conical refraction and optical knots are discovered.

By integrating the transfer function of our custom-developed optical instruments, we have also successfully reproduced and further explored numerous experimental results. This forward model is also inversely applied for inverse focal design in high N.A. laser writing. Lastly, we offer some initial demonstrations of the potential future applications of this powerful LCO model in NCO, including chiral second harmonic conical refraction.

Such a novel paradigm (the M-M TC and crystal-2f system) and the newly discovered phenomena will inject theoretical and experimental vitality into crystal optics, breathing new life into its future. It also lays a solid foundation for all upper-level architectures based on light-matter interactions and will inspire a fresh wave of rethinking in all wave theories, including quantum optics/mechanics.

In addition to developing NCO models based on this LCO framework, we are also actively exploring new solutions to the LCO model itself. This includes investigating alternative (non-rectangular, non-spherical) coordinate systems or retaining Berry’s “South-Pole Stereographic Projection” coordinate system while utilizing non-uniform FT[56] of type 2 (and 1) — sampling non-uniform \bar{k}_ρ grid in 2D reciprocal space while uniformly sampling $\bar{\rho}$ grid in 2D real space to avoid solving transcendental equations.

As an advanced version of wave optics in isotropic free space — an area older than crystal optics itself, crystal optics inherits all of its challenges and extensions. Examples include introducing the (Chriped) Z transform[50], Bluestein algorithm[57], scaled angular spectrum[51], and semi-analytical FT[58] into FCO, enabling adaptive field-of-view(FOV) or ROI scaling in real and reciprocal spaces as a function of propagation distance z , delaying the onset of aliasing errors, and reducing computational complexity in both time and space, all while satisfying the Nyquist sampling theorem.

It is worth emphasizing that similar problem remains at the forefront of the intersection between mathematics and computer science, despite their seemingly simple appearance. That is, achieving fast and accurate semi-numerical implementation to PDEs of highly oscillatory fields and their integral solutions, even in the one-dimensional ordinary differential case, remains a relentless challenge and an enduring pursuit[47].

As a longstanding issue spanning mathematics (linear algebra, PDEs, fractional FT[59], topology), physics (Hamilton’s five great legacies: manifolds, complex numbers, diabolic points, Hamiltonians, quaternions as a whole, Noether’s theorem, and wave optics — the mother of quantum mechanics), and computer science (sampling theorem, butterfly algorithm, Z transform, physical information and convolutional neural networks), along with a scientific “toy gallery” where a simple laser pointer and a small crystal suffice for real-time experiments to verify surrounding objective reality, we hope the “old yet new” aspects of crystal optics will once again attract attention across diverse domains.

4 Methods

4.1 Boundary conditions for laboratory settings

For a commonly used homogeneous dielectric planar slab in laboratory settings, the space dependence of the major material quantity $\bar{\epsilon}'_{rz} := \bar{\epsilon}'_{rz} + \frac{i}{\epsilon_0 \omega} \bar{\sigma}'_z$ (see Supplementary Note 2) is characterized by two step functions[60–62], assuming that the slab is surrounded by isotropic non-chiral transparent media. After establishing the 3D laboratory coordinate system (LCS), also referred to as the \mathcal{Z} frame, whose $+z$ -axis is aligned parallel to the inward normal of the front face of the slab with air as its surroundings, the dielectric tensor of the slab is expressed as[60, 61]

$$\bar{\epsilon}'_{rz} = 1 + (\bar{\epsilon}'_r - 1) \cdot [\text{step}(z) - \text{step}(z - L)] = \begin{cases} \bar{\epsilon}'_r, & 0 < z < L \\ \text{undefined}, & z = 0 \text{ or } z = L \\ 1, & z < 0 \text{ or } z > L \end{cases} \quad (7) \quad 1 \mid 20.$$

Then the wave equation (see Supplementary Note 2), together with Eq. (7), contains all the necessary information for solving the distribution of electromagnetic field inside and outside the slab made of typical optical materials, provided that a two-dimensional(2D) distribution of the vector pump $\bar{E}_{z_0}^\omega$ ('s transverse components $E_{xz_0}^\omega, E_{yz_0}^\omega$) in front of the slab ($z_0 < 0$) is given, which means neither divergence equations[23, 60–66] nor boundary conditions[60, 61] are even required.

If we must assert which boundary conditions are the most fundamental, we would choose the tangential continuity of the electric field \bar{E} and the generalized Snell's law[22, 67] as the sole boundary conditions, due to the general failure of tangential continuity for the magnetic field \bar{H} [60, 61] and the inconvenient use of the normal continuity for the magnetic induction field \bar{B} as its substitute.

The trade-off is that, for each incident field, either two transmission fields passing through the anti-reflective(AR) coating/nanostructure or two reflected fields bounced back by the high-reflective(HR) coating can be calculated relatively accurately, while finer effects such as the photon spin-Hall effect[68, 69] and the additional lateral shift[70] cannot be revealed by this model.

Above boundary conditions adopted in our model naturally align with the standard configuration in modern nonlinear photonics laboratories where slab-shaped crystals with AR/HR coatings/nanostructures applied to both front and rear surfaces are frequently used, rendering our model applicable in the majority of cases.

Besides, regarding the central element of this work, i.e., the 3×2 transition matrix of non-uniform LFCO, since it is defined solely within the material, no extra boundary conditions are required from this standpoint, apart from the generalized Snell's law, which mainly restrains the eigenvalues.

4.2 Eigensystem corrections for phase continuity

The generalized Snell's law between transparent and dissipative/active media with non-Hermitian $\bar{\varepsilon}_r^{\prime\omega}$, will be violated, if one persists in employing uniform plane waves $e^{i\bar{k}^\omega \cdot \bar{r}} = e^{ik_x^\omega \hat{k}_x \cdot \bar{r}} = e^{ik_0^\omega n^\omega \hat{k}_x \cdot \bar{r}}$ with uniform complex wave vectors[15, 16, 25–32, 71]

$$\bar{k}^\omega = k^\omega \hat{k} \in \mathbb{C}_r \times \mathbb{R}_\Theta^2 \subsetneq \mathbb{C}_\lambda^3 \quad (8)$$

across the slab material ($z < 0 \rightarrow z > L$). Because when sticking to this form, transverse wave vectors $k_x^\omega, k_y^\omega = k^\omega \hat{k}_x, k^\omega \hat{k}_y \in \mathbb{C}$ are generally complex and ω -dispersive on the material side (with $\bar{\varepsilon}_r^{\prime\omega}$ and $0 < z < L$), whereas in air surroundings (where $\varepsilon_r = 1$ and $z < 0$ or $> L$) and FT they remain real and non- ω -dispersive, breaking the in-plane momentum conservation = phase continuity, one-to-one correspondence for each plane wave across interfaces and the requirement of FT.

By contrast, adhering to non-uniform complex wave vectors

$$\bar{k}^\omega = \bar{k}_\perp + \bar{k}_z^\omega \xrightarrow[\bar{k}_\perp = \bar{k}_{z\perp}^\omega]{\bar{k}_R^\omega = \bar{k}_\perp + \bar{k}_{zR}^\omega} \bar{k}_R^\omega + i\bar{k}_I^\omega \quad (9a)$$

$$= \bar{k}_R^\omega + i\bar{k}_I^\omega \xrightarrow[\bar{k}_z^\omega = \bar{k}_{zR}^\omega + i\bar{k}_I^\omega]{\bar{k}_\perp = \bar{k}_{R\perp}^\omega} \bar{k}_\perp + \bar{k}_z^\omega \in \mathbb{R}_\perp^2 + \mathbb{C}_Z \quad (9b) \quad 1 \mid 22.$$

One can unravel this coupling by first discarding the imaginary part \bar{k}_I^ω of the complex non-uniform wave vector $\bar{k}^\omega = \bar{k}_R^\omega + i\bar{k}_I^\omega$ in Eq. (9b), retaining only the real part \bar{k}_R^ω 's unit vector \hat{k} from Eq. (10a) as the ray direction in \mathbf{k} space. The input variable \hat{k} is then inserted into Eq. (10b) to form a transcendental equation $k_z^\omega = \sqrt{k_{0\omega}^2 n_\omega^2 (\mathcal{N} \{ \text{Re} [(\bar{k}_\rho, k_z^\omega)^\top] \})} - k_\rho^2$ which asymptotically converges to the ground true eigenvalue $k_z^\omega(\bar{k}_\rho)$ of the booker quartic on condition that

$$|\bar{k}_I^\omega| \ll |\bar{k}_R^\omega|, \quad (11) \quad 1 \mid 22.$$

where material absorption is sufficiently low with typically $k_I^\omega < k_R^\omega \cdot 10^{-3}$ when a transmission spectrum is still present, as exemplified by breiner's laser crystal[32, 39] in Fig. 4b,e.

Berry's input variable \hat{k} can be obtained from Fig. 9a2 as an intermediate data. Inserting it into Fig. 9b yields Berry's eigensystem $n'^\omega(\hat{k}), \bar{d}'_\theta\phi(\hat{k})$, where the eigenvector $\bar{d}'_\theta\phi(\hat{k})$ also converges to the ground truth $\bar{g}^\omega(\bar{k}_\rho)$ under the condition of Eq. (11) (see Supplementary Note 2.2), after undergoing the operation shown in Fig. 9c.

4.3 Overall flowchart of this model

Tables 1 and 2 briefly presents the categorical meanings of the graphical elements (nodes and arrows) as 'CLASSES' in Figs. 1, 9 and 10. The physical/mathematical significance of the specific instantiated 'OBJECTS' within each 'CLASS' can be found in the Supplementary Notes.

Quoted @ 3 pp.
21, 22, 23.

Table 1 The definitions of styles of nodes within Figs. 1, 9 and 10.

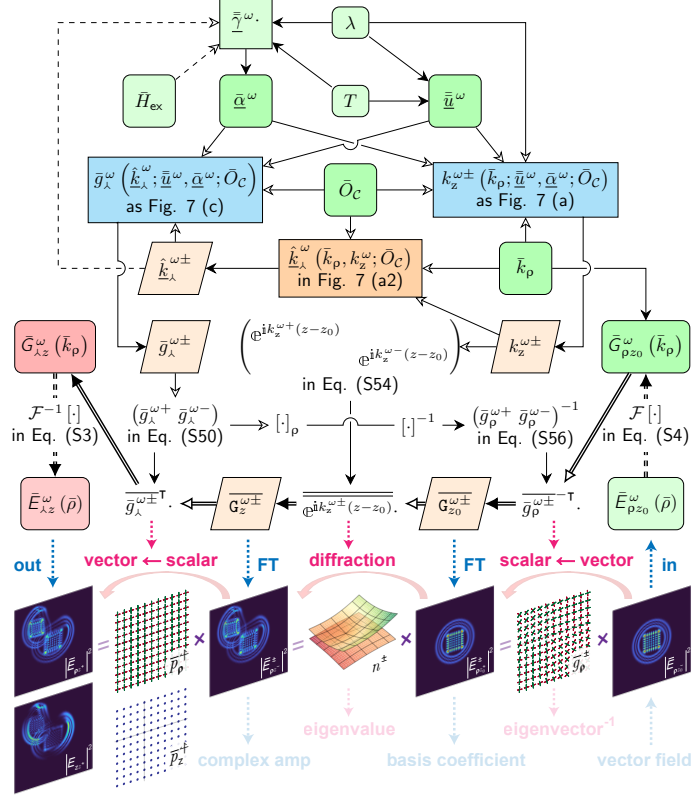
Intermediate Node: Switch Flow	\diamond	conditionally	in a	flowchart	as	<i>if</i>
Initial void Node: Main Origin	\square	at the start of a	flowchart	as its	<i>entry</i>	
Intermediate Data: Private Var	\square	can't be used by	other	flowcharts		
Intermediate Data: Public Var	\square	may be used by	other	flowcharts	as	\square / \square
Initial input Data: Parameter	\square	at the start of a	flowchart	as its	<i>*args</i>	
Initial input Data: Parameter	\square	from within	another	flowchart	as its	\square
Final output Data: Result	\square	at the end of a	flowchart	as its	<i>return</i>	
Intermediate Function/Operator	\square	from (within) / as an	equation			
Intermediate Function/Operator	\square	from / as another	flowchart	as its	$\square(\cdot)$	
Intermediate Function/Operator	\square	from within	another	flowchart	as its	$\square(\cdot)$

Quoted @ 3 pp.
21, 22, 23.

Table 2 The meanings of styles of arrows within Figs. 1, 9 and 10.

Main streams	\Rightarrow	and	\Rightarrow	all equal to	<u>Data</u> as the input of <u>Operator</u>
Side streams	\rightarrow	and	\rightarrow		
Main streams	\Rightarrow	and	\Rightarrow	all equal to	<u>Operator</u> returns its output of <u>Data</u>
Side streams	\rightarrow	and	\rightarrow		or: <u>Data</u> as a Function of <u>Data</u>
					or: <u>Operator</u> as a Function of <u>Operator</u>

Starting from the atomic inputs, we built the comprehensive workflow diagram in Fig. 10 from the bottom up, referencing three submodules from Fig. 9a,c. All elements in the flowcharts (Figs. 1, 9 and 10) of this article are accompanied by step-by-step derivations and detailed explanations provided in the Supplementary Notes.



Quoted @ 7 pp.
21, 22, 22, 22,
23, 23, 26.

Fig. 10 Main flowchart to build the transition matrix in Eq. (5) and Fig. 1 from basic elements. Atomic inputs include the orientation \bar{O}_C of the principal coordinate system (PCS) = the C frame, optical activity tensor $\bar{\gamma}^\omega$ [15], optical activity vector $\bar{\alpha}^\omega$ [72], the symmetric part \bar{u}^ω of $\bar{\epsilon}'_{rz}{}^{-1}$, all initially in the C frame $\bar{\gamma}^\omega, \bar{\alpha}^\omega, \bar{u}^\omega$, together with external magnetic field \bar{H}_{ex} , wavelength λ of monochromatic light, temperature T of the crystal, spatial frequency \bar{k}_ρ , and the input vector pump $\bar{E}_{\rho z_0}^\omega(\bar{\rho})$ in 2D real space. For the meanings of styles of nodes & arrows, see Tables 1 and 2.

Quoted @ 1 p.
26.

4.4 Computational limitation 1 of this model

For transverse spatial frequencies exceeding the wavevector within the medium, i.e. $|\bar{k}_\rho| > k_R^\omega$, the eigensystems should ideally be obtained by solving the Booker quartic and substituting its eigenvalues into the nullspace of the 3×3 characteristic matrix $k_\omega^2 - \bar{k}^\omega \bar{k}_\omega^\top - k_{0\omega}^2 \bar{\epsilon}'_{rz}$ in Eq. (2) to produce the eigenvectors, rather than directly

employing the eigensystems in the southern hemisphere of “South-Pole Stereographic Projection” coordinate system like us. However, since k_z^ω already becomes purely imaginary in this case, resulting in exponential decay along the propagation (z) direction. This approximation is not expected to affect the computational results at depths of several wavelengths. Above adjustment allows our model to accurately simulate the propagation process along the z-axis while depicting eigenstates extending beyond the 2π solid angle (half space).

When the \bar{k}_ρ grid sampling approaches the N.A. limit $= N^\omega$, where $k_\rho \approx k_R^\omega$, the transverse nature of light leads to the eigen-polarizations $\bar{g}_\lambda^{\omega\pm}$ of electric field lacking one of two transverse degree of freedom, with the remaining transverse components $\bar{g}_\rho^{\omega\pm}$ of the two modes parallel $\bar{g}_\rho^{\omega+} \parallel \bar{g}_\rho^{\omega-}$. This makes the inverse of the 2×2 polarization state matrix $\overline{\bar{g}_\rho^{\omega\pm}}^{-T}$ infinite, resembling but differing from the situation at EPs, where $\det(\overline{\bar{g}_\rho^{\omega\pm}}) \rightarrow \infty$ due to $\bar{g}_\lambda^{\omega+} \parallel \bar{g}_\lambda^{\omega-}$. To ensure numerical stability for light propagation calculations outside eigenanalysis, we implemented a safeguard by freezing the eigenstates in this small range $k_R^\omega \cdot (1 - \delta) < k_\rho < k_R^\omega \cdot (1 + \delta)$ to those valid on the nearest border of the critical region. This typically creates an elliptical strip defined by radial nearest-neighbor interpolation for non-hyperbolic material.

The non-rigorous engineering-style treatment described above is effective for Z-direction propagation but invalid for surface waves[66, 73, 74] propagating transversely in XY plane. Additionally, under high N.A. conditions, the reflectivity of s- and p-polarizations is a nonlinear function of the incidence angle, typically either monotonically increasing or decreasing initially before monotonically rising again. As a result, Brewster angle effects may occur near the outer regions of the aperture. Furthermore, when the material is surrounded by a high-refractive-index medium (rather than air), total reflection can arise beyond the critical angle, which renders our treatment of eigensystems in regions near the N.A. limit unphysical and unnecessary. Our model, due to the lack of continuity in the magnetic field \bar{H} , does not account for these aspects, leading to certain loss in accuracy and omission of intriguing phenomena such as the photon spin-Hall effect[68, 69] and the additional lateral shift[70] in both reflection and transmission geometry and in both real and reciprocal space.

Nevertheless, the problems caused by boundary conditions are not the core subject of this paper, which centers on the transition matrix inside the material. And above limitations will be rectified in our next-generation LCO model, albeit at the expense of theoretical elegance.

4.5 Computational limitation 2 of this model

Hyperbolic materials and the strongly anisotropic materials they signify require relatively higher iteration counts in eigenvalue computations, as illustrated in Fig. 5b. If the isofrequency surfaces associated with these materials undergo intense undulations with respect to \hat{k}_R^ω , direct iteration to attain Fourier optical eigenvalues in \bar{k}_ρ domain for regions with sufficiently high N.A. will fail to converge. The non-uniform FT[56] method, mentioned in the Discussion section, offers a potential solution to this limitation. Nevertheless, a new challenge arises for all FCO models: as k_z^ω surface deviates further away from the plane, the accumulated propagation phase differences among Fourier components grow significantly, quickly reaching the limits imposed by the sampling theorem. This classic computational problem for ASM in free-space diffraction — where achieving both high N.A. and long propagation distances is unattainable under a fixed sampling resolution — compounded by the anisotropy of the material, further exacerbates difficulties in simultaneously achieving accurate, rapid, and large-scale computations of vector electromagnetic field distributions in FCO.

4.6 Visualization for eigenvector field on 2D manifold

The paired eigenpolarization states $\bar{g}_\lambda^{\omega\pm}$, represented as double ellipses sharing the same $\bar{k}_\rho \in \mathbb{R}_\perp^2$ in a 2D distribution, are 3D vector complex fields $\in \mathbb{C}^3$. Therefore, in terms of visualization, these ellipses could ideally be depicted on the surface of more general 2D manifolds $\in \mathbb{R}_Z(\mathbb{R}_\perp^2)$ (which does not necessarily have to be planes) embedded in 3D real \bar{k} space $\in \mathbb{R}^3$.

To better illustrate the transverse nature of the vector optical field relative to the wave vector \hat{k}_R^ω , eigen-polars should be depicted on $k_R^{\omega\pm}(\bar{k}_\rho)$ surfaces or its alternative $N_\pm^\omega(\bar{k}_\rho)$, rather than on a \bar{k}_ρ grid plane, as demonstrated by McLeod & Wagner[23].

However, for simplicity, we instead represent them in 2D \bar{k}_ρ domain on a plane (rather than on paired eigenvalue surfaces $N_\pm^\omega(\bar{k}_\rho)$) by retaining the original ellipticity while using only the azimuthal angle φ of the ellipses' major axes in spherical \mathcal{Z} frame.

4.7 Visualization for vector electric fields on 2D manifolds

The transverse property of the light field allows the 3D complex vector optical field $\in \mathbb{C}^2$, distributed in a 2D x, y plane at $z = z_0$, to be expressed and compressed into a 2D distributed 2D complex vector field (considering only its x- and y-components). As the vector synthesis of two orthogonally polarized complex scalar fields undergoing non-interfering independent 2D vibrations, should theoretically comprise four real scalar fields: two amplitudes and two phases. To fully encapsulate this information in a single image, an RGB image with an alpha channel could be used to describe the intensity and phase distribution of one “equivalent complex amplitude field” (= a “RGBA picture.png”), treating it as the basis coefficient $E_z^{\omega p}(\bar{\rho})$. The other “equivalent complex amplitude field” as a mask overlaid on the top layer[75] could be visualized as an “equivalent polarization ellipse field” (= an “ellipse collection.svg”) with identical

initial phases, serving as the basis $\bar{E}_{\rho z}^{\omega p}(\bar{\rho})$, — analogous to how a single mode field $\bar{G}_{\lambda z}^{\omega p} = \bar{g}_{\lambda}^{\omega p} \mathbf{G}_z^{\omega p}$ in Figs. 1 and 10 is composed of its eigenvector $\bar{g}_{\lambda}^{\omega p}$ and complex amplitude $\mathbf{G}_z^{\omega p}$, where $p = +, -$. Although this $\mathbb{C}^2 = \mathbb{C}_{\parallel} \times \mathbb{C}_{\perp} \rightarrow \mathbb{C}_{\text{coeff}} \times \mathbb{C}_{\text{basis}}$ has been largely implemented in Fig. 7c1 in reciprocal space, it has yet to be thoroughly implemented throughout the article, especially in real space.

Motivated by the challenges described in Section 4.4 and the insights provided by the visualization technique in reciprocal space from Section 4.5, attention could be shifted to fields distributed on non-planar propagating general 2D manifolds[76] $\in \mathbb{R}_z^Z(\mathbb{R}_{\perp}^2)$ in 3D real \bar{r} space — e.g. solving wave equation on isophase surfaces that evolve with propagation distance z .

Supplementary information.

- [Supplementary Notes.pdf](#)
- [Supplementary Video 1.1: inner_rings_of_fig.2_0.1s.mp4](#)
- [Supplementary Video 1.2: inner_rings_of_fig.2_0.5s.mp4](#)
- [Supplementary Video 2.1: outer_ring_of_fig.2_0.1s.mp4](#)
- [Supplementary Video 2.2: outer_ring_of_fig.2_0.5s.mp4](#)

Acknowledgements. We thank Sir M.V. Berry for the insights shared through both our online and offline exchanges.

Declarations

- **Funding** This work was supported by the Natural Science Foundation of Jiangsu Province (BK20240005) and the Fundamental Research Funds for the Central Universities (021314380268).
- **Competing interests** The authors declare no competing interests.
- **Data availability** All data generated by this LCO model, along with the parameter file for reconstructing any (sub)figure, can be requested from the first author.
- **Code availability** The trilogy, including scalar/vector L/NFCO, as a whole, will be entirely open-sourced upon the completion of the trilogy.
- **Author contribution** C.X. proposed and led the project. Y.Z. supervised and supported the project.

References

- Cited @ 3 pp. | 2, 5, 9.
- [1] Ossikovski, R., Arteaga, O. & Sturm, C. Constitutive relations for optically active anisotropic media: A review **2**, 2100160. URL <https://onlinelibrary.wiley.com/doi/10.1002/adpr.202100160>.
- [2] Dmitriev, V. G. Effective nonlinearity coefficients for three-wave interactions in biaxial crystals of mm2 point group symmetry . Cited @ 4 pp. | 2, 16, 17, 17.
- Cited @ 7 pp. | 2, 16, 16, 17, 17, 17, 17.
- [3] Diesperov, K. V. & Dmitriev, V. G. Effective nonlinear coefficient for sum-frequency generation with collinear phase matching calculated taking account of the birefringence in biaxial crystals **27**, 433–436. URL <https://iopscience.iop.org/article/10.1070/QE1997v027n05ABEH000966>.
- [4] Grundmann, M. *et al.* Optically anisotropic media: New approaches to the dielectric function, singular axes, microcavity modes and Raman scattering intensities **11**, 1600295. URL <https://onlinelibrary.wiley.com/doi/10.1002/pssr.201600295>. Cited @ 2 pp. | 2, 17.
- Cited @ 1 p. | 3.
- [5] Xu, X. *et al.* Femtosecond laser writing of lithium niobate ferroelectric nanodomains **609**, 496–501. URL <https://www.nature.com/articles/s41586-022-05042-z>.
- [6] Wei, D. *et al.* Experimental demonstration of a three-dimensional lithium niobate nonlinear photonic crystal **12**, 596–600. URL <http://www.nature.com/articles/s41566-018-0240-2>. Cited @ 1 p. | 3.
- Cited @ 1 p. | 3.
- [7] Xu, T. *et al.* Three-dimensional nonlinear photonic crystal in ferroelectric barium calcium titanate **12**, 591–595. URL <http://www.nature.com/articles/s41566-018-0225-1>.
- [8] Keren-Zur, S. & Ellenbogen, T. A new dimension for nonlinear photonic crystals **12**, 575–577. URL <http://www.nature.com/articles/s41566-018-0262-9>. Cited @ 1 p. | 3.
- Cited @ 1 p. | 3.
- [9] Chen, P. *et al.* Quasi-phase-matching-division multiplexing holography in a three-dimensional nonlinear photonic crystal **10**, 146. URL <https://www.nature.com/articles/s41377-021-00588-5>.
- [10] Chen, P. *et al.* Laser nanoprinting of 3D nonlinear holograms beyond 25000 pixels-per-inch for inter-wavelength-band information processing **14**, 5523. URL <https://www.nature.com/articles/s41467-023-41350-2>. Cited @ 1 p. | 3.
- Cited @ 1 p. | 3.
- [11] Berreman, D. W. Optics in Stratified and Anisotropic Media: 4×4-Matrix Formulation **62**, 502. URL <https://opg.optica.org/abstract.cfm?URI=josa-62-4-502>.
- [12] Stallinga, S. Berreman 4×4 matrix method for reflective liquid crystal displays **85**, 3023–3031. URL <https://pubs.aip.org/jap/article/85/6/3023/178429/Berreman-4-4-matrix-method-for-reflective-liquid>. Cited @ 2 pp. | 3, 3.

- | | | |
|---|---|-----------------------------------|
| Cited @ 2 pp.
3, 3. | [13] Moler, C. & Van Loan, C. Nineteen dubious ways to compute the exponential of a matrix, twenty-five years later 45 , 3–49. URL http://epubs.siam.org/doi/10.1137/S00361445024180 . | |
| | [14] Zarifi, D., Soleimani, M. & Abdolali, A. Plane Wave Reflection and Transmission from Uni- and Bi- Axial Chiral Slabs 10 . | Cited @ 1 p.
3. |
| Cited @ 7 pp.
3, 5, 8, 9, 17, 20,
23. | [15] Berry, M. V. & Dennis, M. R. The optical singularities of birefringent dichroic chiral crystals 459 , 1261–1292. URL https://royalsocietypublishing.org/doi/10.1098/rspa.2003.1155 . | |
| | [16] Berry, M. The optical singularities of bianisotropic crystals 461 , 2071–2098. URL https://royalsocietypublishing.org/doi/10.1098/rspa.2005.1507 . | Cited @ 5 pp.
3, 5, 5, 20, 20. |
| Cited @ 3 pp.
3, 3, 3. | [17] Borzdov, G. N. Waves with linear, quadratic and cubic coordinate dependence of amplitude in crystals 46 , 245–257. URL http://link.springer.com/10.1007/BF02846911 . | |
| | [18] Sturm, C. Electromagnetic waves in crystals: The presence of exceptional points 5 , 2300235. URL https://onlinelibrary.wiley.com/doi/abs/10.1002/adpr.202300235 . | Cited @ 2 pp.
3, 4. |
| Cited @ 1 p.
3. | [19] Olyslager, F. & Lindell, I. Electromagnetics and exotic media: A quest for the holy grail 44 , 48–58. URL http://ieeexplore.ieee.org/document/1003634/ . | |
| | [20] Berry, M. & Jeffrey, M. in <i>Chapter 2 Conical diffraction: Hamilton’s diabolical point at the heart of crystal optics</i> , Vol. 50 13–50 (Elsevier). URL https://linkinghub.elsevier.com/retrieve/pii/S0079663807500028 . | Cited @ 1 p.
3. |
| Cited @ 2 pp.
4, 21. | [21] Wang, Y., Liang, L., Xin, H. & Wu, L. Complex ray tracing in uniaxial absorbing media 25 , 653. URL https://opg.optica.org/abstract.cfm?URI=josaa-25-3-653 . | |
| | [22] Chang, P. C., Walker, J. & Hopcraft, K. Ray tracing in absorbing media 96 , 327–341. URL https://linkinghub.elsevier.com/retrieve/pii/S002240730500066X . | Cited @ 4 pp.
4, 20, 21, 21. |
| Cited @ 3 pp.
4, 20, 25. | [23] McLeod, R. R. & Wagner, K. H. Vector Fourier optics of anisotropic materials 6 , 368. URL https://opg.optica.org/aop/abstract.cfm?uri=aop-6-4-368 . | |
| | [24] Kirillov, O. N., Mailybaev, A. A. & Seyranian, A. P. Unfolding of eigenvalue surfaces near a diabolic point due to a complex perturbation 38 , 5531–5546. URL https://iopscience.iop.org/article/10.1088/0305-4470/38/24/007 . | Cited @ 2 pp.
4, 7. |
| Cited @ 2 pp.
5, 20. | [25] Chen, H. C. A coordinate-free approach to wave propagation in anisotropic media 53 , 4606–4609. URL http://aip.scitation.org/doi/10.1063/1.331382 . | |
| | [26] Gerardin, J. & Lakhtakia, A. Conditions for Voigt wave propagation in linear, homogeneous, dielectric mediums 112 , 493–495. URL https://linkinghub.elsevier.com/retrieve/pii/S0030402604700807 . | Cited @ 2 pp.
5, 20. |

- Cited @ 2 pp. | [27] Ossikovski, R. & Arteaga, O. Extended yeh's method for optically active anisotropic layered media **42**, 3690. URL <https://opg.optica.org/abstract.cfm?URI=ol-42-18-3690>.
- [28] Chang, C.-M. & Shieh, H.-P. D. Simple Formulas for Calculating Wave Propagation and Splitting in Anisotropic Media **40**, 6391. URL <https://iopscience.iop.org/article/10.1143/JJAP.40.6391>. | Cited @ 2 pp. 5, 20.
- Cited @ 2 pp. | [29] Zu, R. *et al.* Analytical and numerical modeling of optical second harmonic generation in anisotropic crystals using #SHAARP package **8**, 246. URL <https://www.nature.com/articles/s41524-022-00930-4>.
- [30] Kirillov, O., Mailybaev, A. & Seyranian, A. *On eigenvalue surfaces near a diabolic point*, 319–325 (IEEE). URL <http://ieeexplore.ieee.org/document/1514000/>. | Cited @ 2 pp. 5, 20.
- Cited @ 2 pp. | [31] Grundmann, M. & Sturm, C. The singular optical axes in biaxial crystals and analysis of their spectral dispersion effects in β -Ga₂O₃ **93**, 053839. URL <http://arxiv.org/abs/1601.03760>.
- [32] Brenier, A. Lasing with conical diffraction feature in the KGd(WO₄)₂:Nd biaxial crystal **122**, 237. URL <http://link.springer.com/10.1007/s00340-016-6512-y>. | Cited @ 8 pp. 5, 11, 11, 11, 12, 20, 20, 22.
- Cited @ 1 p. | [33] Grechin, S. G., Nikolaev, P. P. & Okhrimchuk, A. G. Fourier space method for calculating the propagation of laser radiation in biaxial crystals taking into account the angle between the eigenpolarisations **44**, 34–41. URL <http://stacks.iop.org/1063-7818/44/i=1/a=34?key=crossref.c0a29a2463a78f48c3bee05f372ac044>.
- [34] Franta, D. & Vohánka, J. r. Constitutive equations describing optical activity in theory of dispersion **38**, 553–561. URL <https://opg.optica.org/josab/abstract.cfm?uri=josab-38-2-553>. | Cited @ 1 p. 9.
- Cited @ 1 p. | [35] Multunas, C., Grieder, A., Xu, J., Ping, Y. & Sundararaman, R. Circular dichroism of crystals from first principles **7**, 123801. URL <https://link.aps.org/doi/10.1103/PhysRevMaterials.7.123801>.
- [36] Peet, V. Experimental study of internal conical refraction in a biaxial crystal with Laguerre–Gauss light beams **9**. | Cited @ 2 pp. 10, 11.
- Cited @ 4 pp. | [37] Schell, A. J. & Bloembergen, N. Laser studies of internal conical diffraction II Intensity patterns in an optically active crystal, α -iodic acid* **68**, 1098. URL <https://opg.optica.org/abstract.cfm?URI=josa-68-8-1098>.
- [38] Pancharatnam, S. The propagation of light in absorbing biaxial crystals: II. Experimental **42**, 235–248. URL <http://link.springer.com/10.1007/BF03053511>. | Cited @ 4 pp. 11, 11, 11, 12.
- Cited @ 5 pp. | [39] Brenier, A. Voigt wave investigation in the KGd(WO₄)₂:Nd biaxial laser crystal **17**, 075603. URL <https://iopscience.iop.org/article/10.1088/2040-8978/>

17/7/075603.

- [40] Brenier, A., Majchrowski, A. & Michalski, E. Chirality versus dichroism: Competition and role in conical diffraction displayed from the Nd:Bi₂ZnOB₂O₆ acentric biaxial laser crystal **72**, 813–820. URL <https://linkinghub.elsevier.com/retrieve/pii/S0925346717304809>. Cited @ 4 pp. *11, 11, 11, 11*.
- Cited @ 2 pp. *11, 12*. [41] Ballantine, K. E., Donegan, J. F. & Eastham, P. R. Conical diffraction and the dispersion surface of hyperbolic metamaterials **90**, 013803. URL <https://link.aps.org/doi/10.1103/PhysRevA.90.013803>.
- [42] Zhang, S., Partanen, H., Hellmann, C. & Wyrowski, F. Non-paraxial idealized polarizer model **26**, 9840. URL <https://opg.optica.org/abstract.cfm?URI=oe-26-8-9840>. Cited @ 2 pp. *11, 13*.
- Cited @ 2 pp. *11, 13*. [43] Berry, M. V., Jeffrey, M. R. & Mansuripur, M. Orbital and spin angular momentum in conical diffraction **7**.
- [44] Tang, Y. *et al.* Harmonic spin-orbit angular momentum cascade in nonlinear optical crystals URL <http://www.nature.com/articles/s41566-020-0691-0>. Cited @ 3 pp. *11, 13, 13*.
- Cited @ 1 p. *14*. [45] Zusin, D. H. *et al.* Bessel beam transformation by anisotropic crystals **27**, 1828. URL <https://opg.optica.org/abstract.cfm?URI=josaa-27-8-1828>.
- [46] Lin, J., Rodríguez-Herrera, O. G., Kenny, F., Lara, D. & Dainty, J. C. Fast vectorial calculation of the volumetric focused field distribution by using a three-dimensional Fourier transform. Cited @ 1 p. *14*.
- Cited @ 2 pp. *15, 19*. [47] Agocs, F. J. & Barnett, A. H. An Adaptive Spectral Method for Oscillatory Second-Order Linear ODEs with Frequency-Independent Cost **62**, 295–321. URL <https://epubs.siam.org/doi/10.1137/23M1546609>.
- [48] Wang, Z., Baladron-Zorita, O., Hellmann, C. & Wyrowski, F. Theory and algorithm of the homeomorphic fourier transform for optical simulations **28**, 10552. URL <https://opg.optica.org/abstract.cfm?URI=oe-28-7-10552>. Cited @ 1 p. *15*.
- Cited @ 1 p. *15*. [49] Wright, L. G. *et al.* Deep physical neural networks trained with backpropagation **601**, 549–555. URL <https://www.nature.com/articles/s41586-021-04223-6>.
- [50] Leutenegger, M., Rao, R., Leitgeb, R. A. & Lasser, T. Fast focus field calculations. Cited @ 2 pp. *15, 19*.
- Cited @ 2 pp. *15, 19*. [51] Heintzmann, R., Loetgering, L. & Wechsler, F. Scalable angular spectrum propagation **10**, 1407–1416. URL <https://opg.optica.org/optica/abstract.cfm?uri=optica-10-11-1407>.
- [52] Belyi, V. N. Propagation of high-order circularly polarized Bessel beams and vortex generation in uniaxial crystals **50**, 059001. URL <http://opticalengineering>. Cited @ 2 pp. *16, 17*.

spiedigitallibrary.org/article.aspx?doi=10.1117/1.3572109.

- Cited @ 3 pp.
16, 17, 17.
- [53] Midwinter, J. E. & Warner, J. The effects of phase matching method and of uniaxial crystal symmetry on the polar distribution of second-order non-linear optical polarization **16**, 1135–1142. URL <https://iopscience.iop.org/article/10.1088/0508-3443/16/8/312>.
- [54] Yao, J., Shi, W. & Sheng, W. Accurate calculation of the optimum phase-matching parameters in three-wave interactions with biaxial nonlinear-optical crystals **9**, 891. URL <https://opg.optica.org/abstract.cfm?URI=josab-9-6-891>. Cited @ 3 pp.
16, 17, 17.
- Cited @ 1 p.
16.
- [55] Grant, S. D., Zolotovskaya, S. A., Kalkandjiev, T. K., Gillespie, W. A. & Abdolvand, A. On the frequency-doubled conically-refracted Gaussian beam **22**, 21347. URL <https://opg.optica.org/oe/abstract.cfm?uri=oe-22-18-21347>.
- [56] Barnett, A. H., Magland, J. F. & family=Klinteberg, p. u., given=Ludvig. A parallel non-uniform fast fourier transform library based on an "exponential of semicircle" kernel. URL <http://arxiv.org/abs/1808.06736>. 1808.06736. Cited @ 2 pp.
19, 25.
- Cited @ 1 p.
19.
- [57] Hu, Y. *et al.* Efficient full-path optical calculation of scalar and vector diffraction using the Bluestein method **9**, 119. URL <http://www.nature.com/articles/s41377-020-00362-z>.
- [58] Wang, Z., Zhang, S., Baladron-Zorita, O., Hellmann, C. & Wyrowski, F. Application of the semi-analytical Fourier transform to electromagnetic modeling **27**, 15335. URL <https://opg.optica.org/abstract.cfm?URI=oe-27-11-15335>. Cited @ 1 p.
19.
- Cited @ 1 p.
19.
- [59] Pellat-Finet, P., Durand, P.-E. & Fogret, E. Spherical angular spectrum and the fractional order fourier transform **31**, 3429. URL <https://opg.optica.org/abstract.cfm?URI=ol-31-23-3429>.
- [60] Chen, B. & Nelson, D. F. Wave-vector-space method for wave propagation in bounded media **48**, 15365–15371. URL <https://link.aps.org/doi/10.1103/PhysRevB.48.15365>. Cited @ 5 pp.
19, 19, 20, 20, 20.
- Cited @ 5 pp.
19, 19, 20, 20, 20.
- [61] Nelson, D. F. Deriving the transmission and reflection coefficients of an optically active medium without using boundary conditions **51**, 6142–6153. URL <https://link.aps.org/doi/10.1103/PhysRevE.51.6142>.
- [62] Asoubar, D., Zhang, S. & Wyrowski, F. Simulation of birefringence effects on the dominant transversal laser resonator mode caused by anisotropic crystals **23**, 13848. URL <https://opg.optica.org/abstract.cfm?URI=oe-23-11-13848>. Cited @ 2 pp.
19, 20.
- Cited @ 1 p.
20.
- [63] Landry, G. D. & Maldonado, T. A. Complete method to determine transmission and reflection characteristics at a planar interface between arbitrarily oriented biaxial media **12**, 2048. URL <https://opg.optica.org/abstract.cfm?URI=josaa-12-9-2048>.

- [64] Abdulhalim, I. Exact 2×2 matrix method for the transmission and reflection at the interface between two arbitrarily oriented biaxial crystals **1**, 655–661. URL <https://iopscience.iop.org/article/10.1088/1464-4258/1/6/301>. Cited @ 1 p. 20.
- Cited @ 1 p. 20. [65] Chang, P.-H., Kuo, C.-Y. & Chern, R.-L. Wave propagation in bianisotropic metamaterials: Angular selective transmission .
- [66] Chern, R.-L. & Yu, Y.-Z. Chiral surface waves on hyperbolic-gyromagnetic metamaterials . Cited @ 2 pp. 20, 24.
- Cited @ 2 pp. 20, 21. [67] Dupertuis, M. A. & Proctor, M. Generalization of complex Snell-Descartes and Fresnel laws .
- [68] Ling, X. *et al.* Topology-Induced Phase Transitions in Spin-Orbit Photonics **15**, 2000492. URL <https://onlinelibrary.wiley.com/doi/abs/10.1002/lpor.202000492>. Cited @ 2 pp. 20, 24.
- Cited @ 2 pp. 20, 24. [69] Ling, X. *et al.* Photonic Spin-Hall Effect at Generic Interfaces **17**, 2200783. URL <https://onlinelibrary.wiley.com/doi/abs/10.1002/lpor.202200783>.
- [70] Zhang, Y., Zhang, S., Zheng, Y. & Wang, S. Algorithm for accurate and efficient calculation of coating-induced effects **32**, 29279. URL <https://opg.optica.org/abstract.cfm?URI=oe-32-17-29279>. Cited @ 2 pp. 20, 24.
- Cited @ 1 p. 20. [71] Yeh, P. Electromagnetic propagation in birefringent layered media .
- [72] Landau, L. D. & Lifshitz, E. M. in *CHAPTER XI - ELECTROMAGNETIC WAVES IN ANISOTROPIC MEDIA* (eds Landau, L. D. & Lifshitz, E. M.) *Electrodynamics of Continuous Media (Second Edition)*, Vol. 8 of *Course of Theoretical Physics* 331–357 (Pergamon). Cited @ 1 p. 23.
- Cited @ 1 p. 24. [73] Lakhtakia, A., Mackay, T. G. & Zhou, C. Electromagnetic surface waves at exceptional points **42**, 015302. URL <https://iopscience.iop.org/article/10.1088/1361-6404/abb6c7>.
- [74] Mackay, T. G. & Lakhtakia, A. *Electromagnetic Anisotropy and Bianisotropy: A Field Guide* 2 edn (WORLD SCIENTIFIC). URL <https://www.worldscientific.com/worldscibooks/10.1142/11351>. Cited @ 1 p. 24.
- Cited @ 1 p. 25. [75] Flossmann, F., Schwarz, U. T., Maier, M. & Dennis, M. R. Polarization Singularities from Unfolding an Optical Vortex through a Birefringent Crystal **95**, 253901. URL <https://link.aps.org/doi/10.1103/PhysRevLett.95.253901>.
- [76] Zhang, S., Asoubar, D., Hellmann, C. & Wyrowski, F. Propagation of electromagnetic fields between non-parallel planes: A fully vectorial formulation and an efficient implementation **55**, 529. URL <https://opg.optica.org/abstract.cfm?URI=ao-55-3-529>. Cited @ 1 p. 26.